To the Graduate Council:

I am submitting herewith a thesis written by John Curtis Crawford Jr. entitled "Investigating the Origin of Precambrian Molar-Tooth Carbonate." I have examined the final electronic copy of this thesis for form and content and recommend that it be accepted in partial fulfillment of the requirements for the degree of Master of Science, with a major in Geology.

Linda Kah

Major Professor

We have read this thesis
and recommend its acceptance:

Theodore Labotka

Mostafa Fayek

Accepted for the Council:

Anne Mayhew

Vice Chancellor and
Dean of Graduate Studies

(Original signatures are on file with official student records.)

# INVESTIGATING THE ORIGIN OF PRECAMBRIAN MOLAR-TOOTH CARBONATE

A Thesis

Presented for the

Master of Science Degree

The University of Tennessee, Knoxville

John Curtis Crawford Jr.
May 2006

## ACKNOWLEDGMENTS

This project was funded by grants and scholarships from the Geological Society of America, Society for Sedimentary Geology (SEPM), Sigma Xi, and the University of Tennessee Department of Earth and Planetary Sciences (Graduate Teaching Assistantship).

I thank Dr. Linda Kah for her guidance and inspiration. Also, thanks to Dr. Fayek and Dr. Labotka for their helpful advice. Thanks also to Dr. Bartley for letting me “shack-up” with her while she helped me with ESEM imaging. Dr. Sepaniak, Dr. Geisfeldt and the Raman spectroscopy group at UT (especially Maggie and Peter) are thanked for teaching me everything I know about Raman spectroscopy. A special thanks also goes to Dr. Sumrall for helping with all kinds of different problems.

Special thanks go to my wife Lisa, and my son Ethan; everything I do, I do it for you (Brian Adams 1991).

For Quintin Overocker, thanks for nothin’ you pony-lovin’, freedom-hatin’ dock monkey!

## ABSTRACT

Molar-Tooth (MT) is an enigmatic carbonate structure that consists of a complex array of variously shaped voids filled with an unusual microspar cement. Most current research has been focused on the mechanism of formation of molar-tooth voids, and the leading model suggests a subsurface, soft-sediment, gas escape mechanism. However, little is known about the calcite microspar that fills MT voids. Brittle deformation of MT structures during sediment compaction indicates that lithification of MT voids is essentially synsedimentary. Under cathodoluminescence (CL) microscopy, MT microspar appears as small (3-12 μm), spheroidal to rhombic, non-luminescent cores surrounded by luminescent, isopachous overgrowths. Crystal size distributions (CSD) indicate that microspar cores originated in a spontaneous nucleation event, followed by varying degrees of Ostwald ripening.

Elemental analyses of void-filling microspar (core + rims) indicate that MT microspar is typically low-Mg calcite. SIMS ion imaging however shows that within the microspar, Mg is partitioned into the cores relative to the overgrowths. Laser-Raman spectroscopy confirms current calcite structure, and spectral peaks have half-widths consistent with low Mg-calcite. However, anomalous weak peaks are found in some MT samples. These peaks are located at 180, 200, 225 $cm^{-1}$ and may reflect remnants of a previously unstable mineral phase.

It has been suggested that vaterite may have been the original carbonate precipitate. Vaterite is a highly unstable calcium carbonate polymorph that commonly has a spheroidal crystal morphology and transforms rapidly to rhombic calcite. Penecontemporaneous precipitation of overgrowth cements that preserve spheroidal, transitional, and rhombic crystal forms is consistent with rapid mineralogical transformation. CSDs, SIMS trace element mapping, and Raman spectroscopy are consistent with original vaterite precipitation.

## TABLE OF CONTENTS


| Section | | Page |
|---|---|---|
| I. | INTRODUCTION | 1 |
| | What are MT Structures | 1 |
| | Mechanisms of MT Formation | 3 |
| | Spatial and Temporal Distribution | 5 |
| | This Study | 7 |
| II. | SAMPLE SELECTION | 8 |
| III. | PETROGRAPHIC DESCRIPTION | 9 |
| IV. | METHODS | 16 |
| | Sample Selection | 16 |
| | Elemental and Isotopic Analysis | 16 |
| | Crystal Size Distributions (CSDs) | 17 |
| | SIMS Trace Element Imaging | 18 |
| | Raman Spectroscopy | 19 |
| V. | RESULTS AND INTERPRETATIONS | 20 |
| | Elemental and Isotopic Analysis | 20 |
| | Crystal Size Distributions (CSDs) | 20 |
| | SIMS Analysis | 28 |
| | Raman Spectroscopy | 31 |
| VI. | DISCUSSION | 38 |
| | Model for MT Microspar | 38 |
| | Implications of Analysis | 40 |
| VII. | CONCLUSION | 44 |
| REFERENCES | | 45 |
| VITA | | 50 |

## LIST OF TABLES


| | | |
|---|---|---|
| **Table 1:** | Elemental composition of MT microspar and host rocks. | 21 |
| **Table 2:** | Isotopic composition of MT microspar and host rock. | 22 |
| **Table 3:** | Measured spectral peaks of different calcium carbonate polymorphs. | 33 |
| **Table 4:** | Observed half-widths of various Mg-calcites and MT microspar samples. | 36 |
| **Table 5:** | Distribution coefficients of Mg for various carbonate phases. | 42 |

## LIST OF FIGURES


| | | |
|---|---|---|
| **Figure 1:** | MT structures from the Belt Supergroup, Montana. | 2 |
| **Figure 2:** | MT structures in well-laminated strata, Avzyan Supergroup, Russia. | 4 |
| **Figure 3:** | Transmitted light image of MT microspar. | 10 |
| **Figure 4:** | Transmitted light image of MT structure. | 11 |
| **Figure 5:** | CL images of MT end-members. | 12 |
| **Figure 6:** | CL images of MT microspar from A) China (WSHN-B), B) Mauritania (ATS-163), C, D) Russia (C133-2078.8A and KTTK-10A respectively), and E) Montana (HH01-202). | 13 |
| **Figure 7:** | ESEM secondary electron image of MT microspar. | 15 |
| **Figure 8:** | Elemental composition of MT microspar and host rock. | 23 |
| **Figure 9:** | Theoretical CSD shapes adapted from Eberl et al. (1998). | 24 |
| **Figure 10:** | CSDs for samples selected for this study. | 26 |
| **Figure 11:** | Log-graphs of the cumulative frequency for MT microspar CSDs. | 27 |
| **Figure 12:** | SIMS high-resolution ion mapping. | 29 |
| **Figure 13:** | Typical Raman spectra for each sample. | 34 |
| **Figure 14:** | SEM images of vaterite. | 39 |

# I. INTRODUCTION

Changes in carbonate depositional fabric through the Precambrian are believed to reflect a secular decrease in the carbonate saturation state of marine systems (Grotzinger 1989; Bartley and Kah 2004). An unusual carbonate fabric known as molar-tooth structure (MT) is of particular interest because 1) it occurs globally, 2) it occurs predominantly during the Meso- and Neoproterozoic, and 3) it composes up to 25% of the precipitated carbonate of this time (James et al. 1998). The restricted temporal occurrence and spatial abundance of MT suggest that the formation and preservation of this unusual fabric reflect a particular set of marine geochemical conditions. Therefore, understanding of MT formation and preservation is critical to deciphering the geochemistry of Proterozoic marine systems.

## *What Are MT Structures*

MT structures were first described by Bauermann (1885) as ribbons of calcite that appeared similar to crenulations on the grinding surfaces of the molar teeth of elephants. MT structures (Fig. 1) consist of a complex array of variously shaped voids (mm scale) within fine-grained sedimentary rocks that are filled with an unusual carbonate microspar[1]. The morphology of MT structures varies from linear to sinuous horizontal and vertical ribbons and sheets, to spherical blobs (O'Connor 1972). MT structures measure from sub-millimeter to tens of millimeters in width with continuous, sometimes broken, ribbons often extending for tens of centimeters (Pollock et al. 2006); however, the smallest structures are the most abundant. The various MT structures often intersect, forming a three dimensional network of interconnected structures (Fig.1) (Furniss et al. 1998; Pratt 2001; Pollock et al. 2006; Bishop and Sumner *in revision*).

[1] At the International Conference of IGCP447 on MT structures, it was agreed that the term *molar-tooth structures* should be restricted to blob and crack fills in carbonate strata, with uniform equant-microcrystalline carbonate filling the sharp-walled features (Episodes 2003).

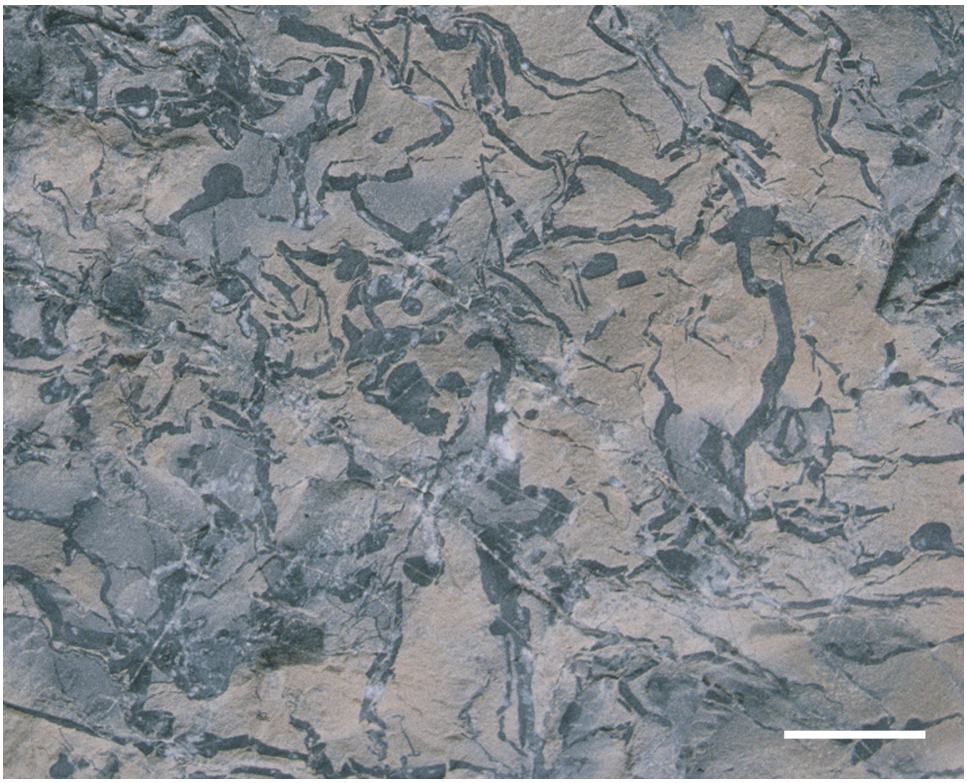

Fig. 1-MT structures from the Belt Supergroup, Montana. Variously shaped ribbons and blobs frequently intersect in three dimensions, forming a complex network of interconnected structures. Scale bar is 3 cm.

Several lines of evidence suggest that precipitation of MT microspar occurred penecontemporaneously with MT structures. MT structures cross-cut sedimentary laminae (Fig. 2), indicating that MT structures formed within the sedimentary substrate prior to compaction. Early studies of MT (Smith 1968; O'Connor 1972) recognized that often sedimentary laminae compacted around MT structures, indicating that MT microspar precipitated within MT voids before compaction of the surrounding sediment (Fig. 2). Compaction evidence suggests that MT voids became lithified within the first meter of the sediment column (Abegg and Anderson 1997; Furniss 1998). Rip-up breccias of MT structure support this and suggest early diagenesis (James et al. 1998). James et al. (1998) suggested that the scarcity of detrital fill indicates that the material preserving the MT voids formed in a synsedimentary fashion. Hofmann (1985) described a carbonate microspar similar to MT microspar that fills organic–walled fossils Chuaria and Tawuia. In this case, microspar must have precipitated prior to decomposition and collapse of cell walls because organic matter typically decomposes in a matter of days (Bartley 1996).

Precipitation of MT microspar within voids may be responsible for preservation of MT structures (Shields 2002). In one outstanding example, carbonate nodules of the Burovaya Formation, Siberia, contain abundant MT structure. Sedimentary laminae are continuous through the nodule, but show greater compaction outside the nodule, suggesting that the nodule (and the MT within) lithified before the surrounding sediment (Pope et al. 2003). Pope et al. (2003) also suggested that MT voids probably formed throughout the substrate, yet were not preserved outside the nodules because they lacked void-filling microspar precipitate.

### *Mechanisms of MT Formation*

Different models for the genesis of MT voids have been proposed, including tectonic fracturing (Daly 1912), sediment compaction (Bell 1966), replacement of algal (O'Connor 1972) and evaporitic (Eby 1977) structures, synaresis (Horodyski 1976; Young and Long 1977; Calver

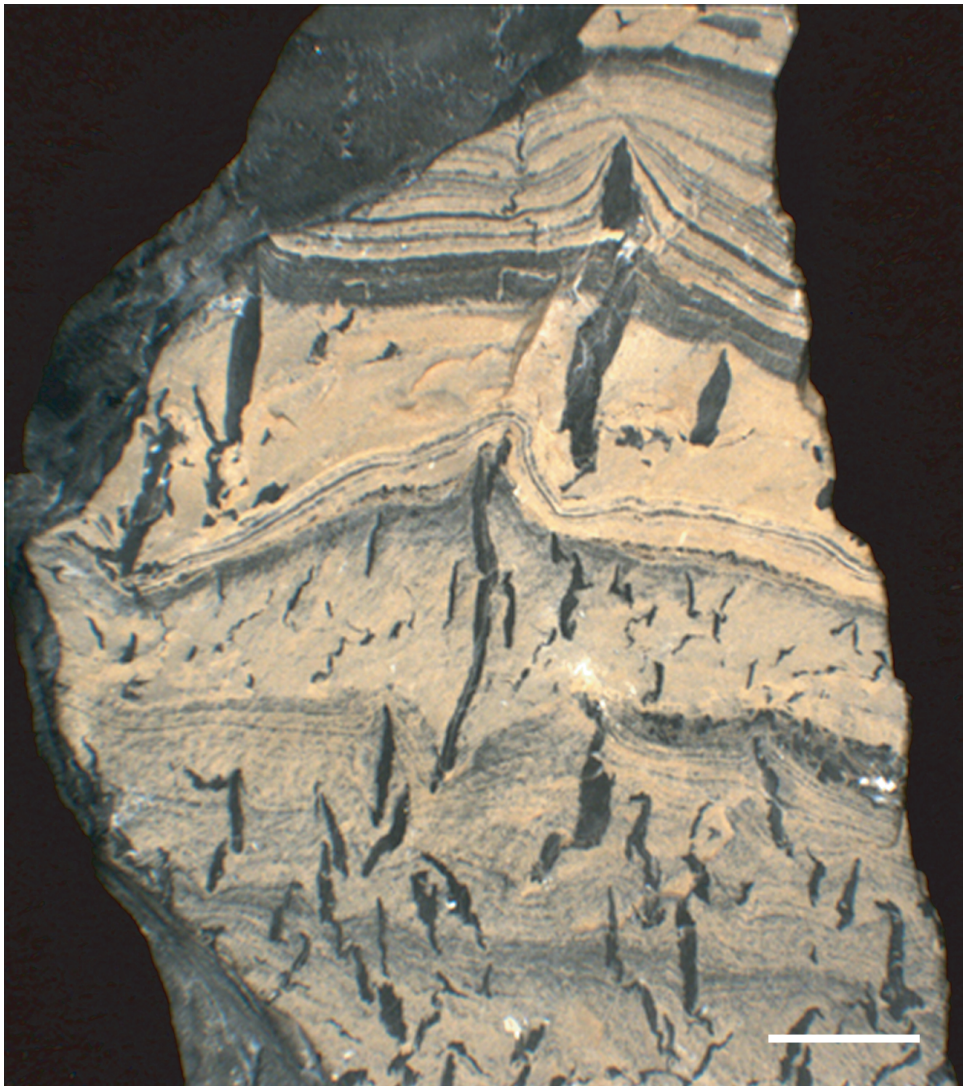

Fig. 2- MT structures in well-laminated strata, Avzyan Supergroup, Russia. Sedimentary laminae show compaction around cross-cutting, dually tapered MT ribbons indicating formation and lithification of MT voids prior to lithification of surrounding sediment. Scale bar is 2 cm.

and Baillie 1990), mudcrack deformation (Demicco and Hardie 1994), earthquake-induced dewatering (Fairchild et al. 1997; Pratt 1998, 2001), and gas expansion and migration (Furniss et al. 1998; Marshall and Anglin 2004; Pollock et al. 2006). However, for a model to fully explain the origin of MT structure, it must account for both the formation of MT voids *and* the rapid precipitation of carbonate microspar within the void space.

Only the gas expansion and migration models (Furniss et al. 1998; Marshall and Anglin 2004, Pollock et al. 2006) can account for both the formation of MT voids and origin of the void-filling microspar. These models suggest that MT structures formed from shallow subsurface gases derived from the decomposition of sedimentary organic matter (OM) by sulfate reduction, methanogenesis, or the destabilization of $CO_2$-clathrates. Gas generated within the substrate would produce spheroidal voids and, if gas pressures exceed cohesion strength of sedimentary substrate, would migrate toward the sediment–water interface leaving crack- and bleb-like voids (Pollock et al. 2006). Supersaturated pore fluids migrating into the voids immediately after gas migration, would then trigger nucleation and precipitation of void-filling microspar (Pollock et al. 2006).

### *Spatial and Temporal Distribution*

Although MT structure has a global paleogeographic distribution, the occurrence of MT structures appears to be constrained both spatially and temporally. MT structures have been found on many stable cratons (five represented in this study), indicating a global paleo-distribution. Most MT structures formed in subtidal to intertidal carbonate ramp and shelf settings in stable cratonic basins (Knoll & Swett 1990; Fairchild et al. 1997; James et al. 1998; Marshall and Anglin 2004). Although MT is frequently associated with storm rip-up breccias, the depth of MT formation may have been below storm wave base (Pratt 1998), or as deep as tsunami wave base, to 200 m depth (Marshall and Anglin 2004). However, James et al. (1998) and Furniss et al.

(1998) suggested that ubiquitous microbial mats are required to "seal" the surface for MT structure to occur. This would likely limit the depth of MT structure formation to storm wave base.

Volumetrically significant MT structure at the formation level (James et al. 1998) is found in every carbonate environment of Meso- and early Neoproterozoic age. Scarcity of MT structures in Archean and early Paleoproterozoic marine deposits likely resulted from the abundance of sea-floor precipitates that characterize Archean and Paleoproterozoic strata (Pollock et al. 2006). In the absence of soft sediment, early Precambrian environments would not be conducive to void formation. Decreased seawater carbonate saturation through the Meso- and Neoproterozoic (c.f. Bartley and Kah 2004; Kah and Knoll 1996) would be more conducive to crack formation (Frank and Lyons 1998; Pollock et al. 2006) because of the presence of abundant soft sediments.

The absence of MT structure in Phanerozoic strata has been attributed to the advent of bioturbation (Horodyski 1976; Fairchild et al. 1997; James et al. 1998; Frank and Lyons 1998). Although bioturbation may have erased similar voids in Phanerozoic deposits, abundant bioturbation did not develop until after 550 Ma, yet volumetrically significant MT disappears around 750 Ma (Shields 2002). Disappearance of MT structures is perhaps more directly linked to the disappearance of the penecontemporaneous void-filling microspar, which is integral in preserving the structure (Shields 2002; Pope et al. 2003; Pollock et al. 2006). Through the Precambrian, MT structure and stromatolite diversity appear to decrease together, further supporting an environmental control. Stromatolite diversity decrease has been interpreted as resulting from a change in seawater composition (Grotzinger 1990; Grotzinger and Knoll 1999). Decreasing carbonate saturation state through the Proterozoic may be the global environmental factor controlling both the appearance and disappearance of void–filling MT microspar, and therefore MT structure.

### *This Study*

The purpose of this study is to define the petrographic, mineralogic, and geochemical character of MT microspar to better understand its genesis and relationship to global Precambrian environmental factors. Petrographic analysis by transmitted-light and cathodoluminescence (CL) microscopy allows characterization of MT microspar, its relationship to MT voids, and recrystallization trends. Crystal size distributions are examined to interpret information about crystal nucleation, nucleation density, and crystal growth rate (Kile et al. 2000). In addition, high-resolution laser-Raman microprobe spectroscopy is used to define the current mineral content and investigate the structure of MT microspar. Raman spectra are characteristic of mineral structure and can reveal disorder (Bischoff et al. 1985) resulting from remnant cation content or structural defects in the crystal structure associated with mineral transformation. Finally, SIMS trace-element mapping provides qualitative data regarding trace element incorporation into the crystal structure. Together, this multi-technique approach provides insight into the origin of this unusual carbonate microspar and may improve understanding of changing carbonate saturation state in the Proterozoic and the precipitation of specific carbonate fabrics.

## II. SAMPLE SELECTION

To gain a broad perspective on the genesis of MT microspar in time and space, samples for this study were selected from five localities representing deposition on five cratons during 700 my of the Proterozoic. These localities include the ~1.4 Ga Helena Formation, Belt Supergroup, Montana (sample HH01-54C and HH01-202; Pollock et al. 2006); the 1.6-1.3 Ga Kyrpin Group, East European Platform (sample C133-2078.8A; Kah et al. *in press*); the ~1.25 Ga Avzyan Group, Russia (sample KTTK-10A; Bartley et al. *in press*); the ~1.2 Ga Atar Group, Mauritania (sample ATS-163; Kah et al. *in preparation*); and the ~750 Ma Jiangsu Province, China (sample WSHN-87 and WSHN B; Xiao *personal communication*).

## III. PETROGRAPHIC DESCRIPTION

Polished thin- and thick-sections were examined by standard petrographic and cathodoluminescence techniques to fully characterize the range of similarities and differences of MT microspar. Luminescence in sedimentary carbonates commonly is activated by the presence of $Mn^{2+}$ within the carbonate structure and is quenched by $Fe^{2+}$ (Hemming et al., 1989). This technique is used as a first-order evaluation of diagenetic alteration because luminescent heterogeneities reflect recrystallization processes, such as zoning resulting from systematic dissolution and precipitation.

In thin-section, MT microspar consists of uniform equant crystals from ~7–15 μm in diameter (Fig. 3). Individual crystals are non-interlocking with sharp crystal boundaries, and contain no evidence of neomorphic recrystallization, suggesting primary precipitation. MT microspar is distinguishable from the surrounding sediment and forms a very sharp contact suggesting *in situ* formation in original void space (Fig. 4). However, lack of grain coarsening inward and lack of competitive growth boundaries suggest that MT microspar does not nucleate on, and grow away from, the void edge as is typical of traditional carbonate cements.

Polished thick sections, viewed under cathodoluminescence, reveal that the uniform equant crystals seen in transmitted light actually consist of two discrete components (Fig. 5, 6): dully luminescent spheroidal to rhombic cores (3-12 μm in diameter), surrounded by an isopachous rim of brightly luminescent material. CL observations reveal subtle transitions in the structure of MT microspar. In some cases, CL reveals MT microspar cores that are mostly round and non-luminescent. By contrast, other samples reveal abundant rhombic cores that exhibit luminescent zoning (Fig. 5b). The majority of samples (Fig. 6) contain both spherical and rhombic cores as well as a variety of intermediate forms. Interestingly, the samples with the most rhombic cores have cores that exhibit luminescent zoning. This suggests that the non-luminescent spheroidal cores are the primary form of crystal precipitated, and the zoned rhombic crystals are a

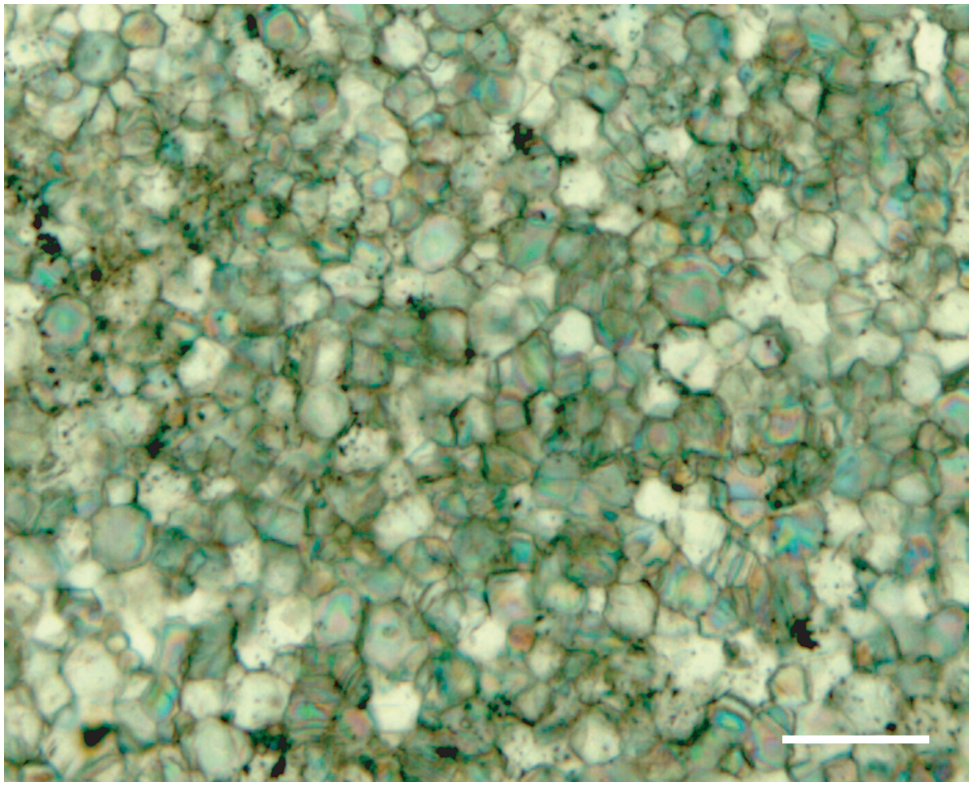

Fig. 3-Transmitted light image of MT microspar. Equant 5-15 μm sized crystals, sharp, planar crystal boundaries, and absence of cloudiness or inclusions suggests a primary precipitation texture, rather than neomorphism. Scale bar is 25 μm.

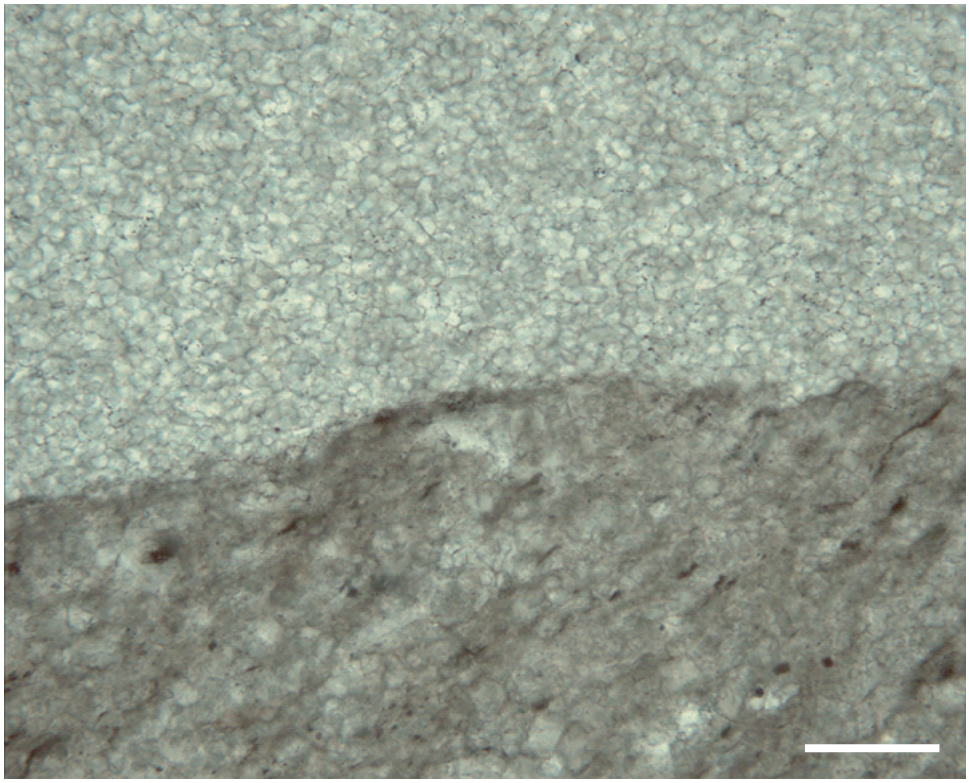

Fig. 4- Transmitted light image of MT structure. MT microspar (top) is distinct from the surrounding matrix. A sharp contact indicates microspar represents filling of original void space, rather than neomorphic recrystallization. Scale bar is 75 μm.

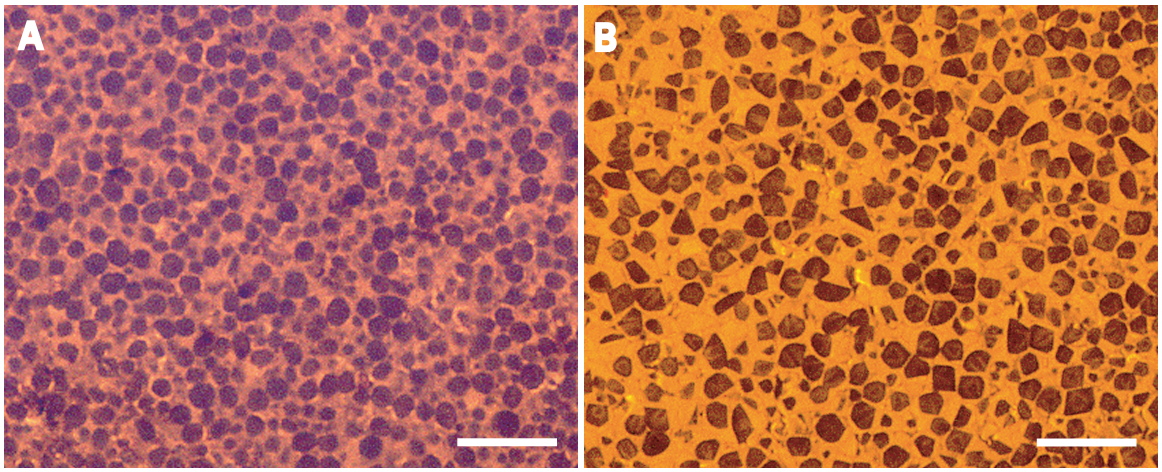


Fig.5- CL images of MT end-members. Images reveal the two-component nature of MT microspar. Isopachous rims of luminescent cement overgrew pre-existing dully luminescent cores. A third generation of non-luminescent cement fills remaining void space. A) Dominantly spheroidal dully luminescent cores (WSHN-87). B) Variously angular cross sections representing transitional to rhombohedral core morphologies (HH01-54C). Luminescent zoning within cores and greater amount of tertiary void space suggest recrystallization in presence of void-filling fluids. Scale bar is 20 μm.

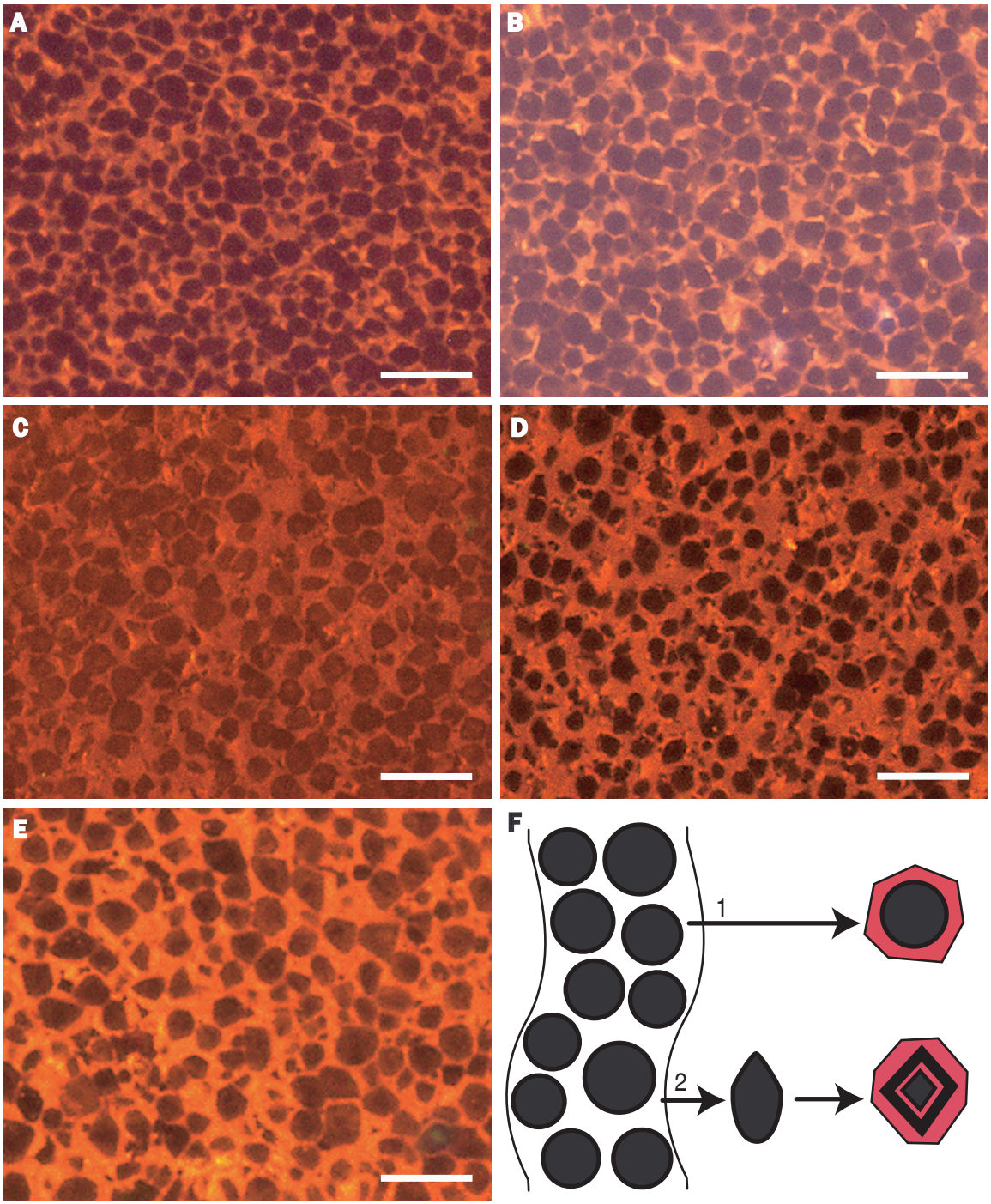


Fig.6- CL images of MT microspar from A) China (WSHN-B), B) Mauritania (ATS-163), C, D) Russia (C133-2078.8A and KTTK-10A respectively), and E) Montana (HH01-202). Images show increasing angularity of microspar cores and increasing luminescent zoning. F) Proposed diagenetic pathways for MT microspar. F1) Spheroidal cores are rapidly entrapped by isopachous overgrowths preserving original morphology, or F2) spheroidal cores undergo transformation prior to precipitation of isopachous overgrowths. Scale bars in A - E are 20 µm.

result of dissolution and reprecipitation. Together, these observations suggest that MT microspar cores may have originally formed as spherical cores, some of which underwent a process of recrystallization to a more stable rhombic form. The process of conversion from spheroidal to rhombic crystal shape must have occurred prior to cementation by the isopachous overgrowths. As such, isopachous overgrowths acted to retain the shape of both rhombic and spheroidal cores, thereby constraining crystal shape during any continued transformation.

Variously shaped MT microspar cores, distinct from corresponding overgrowths, are apparent as well when viewed under Environmental Scanning Electron Microscopy (ESEM). Figure 7 shows sharp contact with surrounding sediment, a variety of core shapes, various degrees of roundness, and isopachous overgrowths evidently using cores as nucleation sites. Although some of these MT cores have experienced transformation to rhombic shape, rhombic cores are Lighter colored and less angular than the rhombic dolomite in the sedimentary matrix.

MT microspar is a synsedimentary void-filling microspar that fills available void space, and lithified rapidly, prior to the surrounding soft sediment. Individual crystals appear to have a three-part growth history. First, isopachous cement rims indicate that non-luminescent cores precipitated in suspension within the void space. Second, some cores recrystallize into more rhombic forms. Third, overgrowth of luminescent material fills remaining void space between cores.

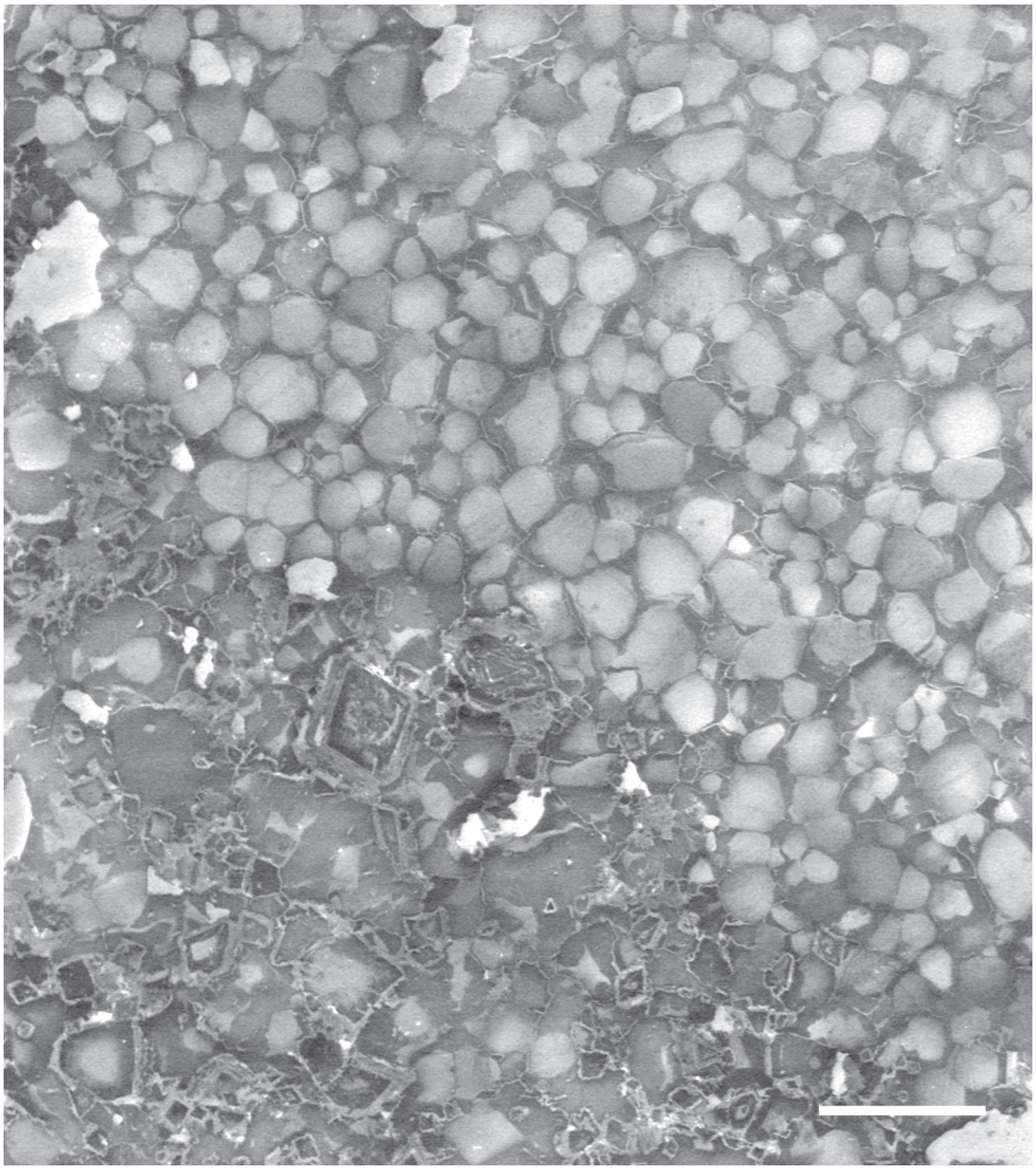

Fig. 7- ESEM secondary electron image of MT microspar. MT microspar (top right) forms a sharp border with surrounding sediment. MT microspar shows a range of core morphologies, various degrees of roundness, and isopachous overgrowths. Scale bar is 20 μm.

## IV. METHODS

### *Sample Selection*

Based on petrographic observations, samples for further analysis were selected from a suite of samples from each location. One sample per location was chosen to reflect the petrographic features characteristic of each locality. China (WSHN-87) and Montana (HH01-54C) were selected as examples of end-member core morphologies (Fig. 5) representing least and most recrystallized cores respectively. This resulted in seven samples (one from each location plus the two end-members), each of which was analyzed via CSD, SIMS, and Raman spectroscopy. Two samples (WSHN-87, C133-2078.8A) and an additional sample (ATS98-13B) were also analyzed for stable isotopes and major and minor element composition.

### *Elemental and Isotopic Analyses*

Bulk MT microspar (core and rims) and the surrounding matrix were each micro-drilled from thick sections of samples from China (WSHN-87), Russia (C133-2078.8A), and Mauritania (ATS98-13B) using 0.5 mm drill bits. For elemental analysis, 2-3 mg sample powder was digested for 2 hours in 5.0 mL of ultrapure 2N $HNO_3$. Solutions were then centrifuged and decanted to avoid insoluble residue. Major and minor element (Ca, Mg, Fe, Mn, and Sr) concentrations were measured at the State University of West Georgia using a Perkin Elmer Inductively Coupled Plasma Optical Emission Spectrometer (ICP-OES) fitted with a Meinhardt nebuliser and calibrated to a series of gravimetrically determined standards. Reproducibility, determined through replicate analysis of sample and standard solutions, is better than 5% for Ca, Mg, Sr, and Mn and better than 10% for Fe.

For stable carbon and oxygen isotope analysis, 0.5 – 1.0 mg sample powder was vacuum sealed and reacted with 110% $H_3PO_4$ at 120°C for 15 minutes in individual reaction vessels of an on-line, automated Finnigan CarboFlo device coupled to a Finnigan Mat Delta Plus (dual inlet)

IRMS. Oxygen isotope ratios were corrected for the isotopic fractionation occurring at 120°C to be comparable to experiments performed at the standard temperature of 30°C. Isotope ratios are reported in per mil (‰) relative to the VPDB (Vienna Pee Dee Belemnite) standard. Precision is better than 0.05‰ for $\delta^{13}C$ and 0.2‰ for $\delta^{18}O$, and was calculated using the ANU P3 (B) standard.

***Crystal Size Distributions (CSDs)***

Crystal size distributions (CSDs) utilize the frequency of crystal sizes to interpret the crystal nucleation and growth history (Eberl et al. 1998). Although application of CSDs has been used mostly for igneous and metamorphic rocks (Cashman and Ferry 1988; Marsh 1988, 1998), Kile et al. (2000) and Eberl et al. (1998) applied CSD models to calcite nucleation and growth experiments. Calcite crystal growth experiments (Kile et al. 2000) and subsequent CSDs compared favorably to the Eberl et al. (1998) theoretical models, suggesting that growth mechanisms can be interpreted by the CSD.

To understand the genesis of these two–part crystals, we chose to measure only cores. For CSD analyses, digital images were obtained using transmitted light microscopy, cathodoluminescence, and ESEM imaging. Each method was tested for precision by replicate measuring of CSDs for a single set of samples. The nature of transmitted light microscopy resulted in error imposed by images that did not distinguish the two phases of crystals and contained ambiguous crystal boundaries. Images from the ESEM gave greatest resolution images for CSD calculations, and distinction between core and overgrowths was possible with all samples. Images were collected from finely polished (0.03 μm) thick-sections by using secondary electron mode with a working distance ~13 mm (600x magnification). Working voltage was 20kV with an internal pressure of 106.7 Pa. However, charging problems resulted in photomicrographs that were distorted, thereby compromising clarity. Cathodoluminescence

produced images that are two-dimensional, and allowed relatively clear distinction between the cores and overgrowths. These revealed data that were most relevant to initial nucleation and growth mechanisms.

CSDs were calculated from crystal size data using the program NIH Image. Diameters through the shortest chord of all individual cores within a square area were measured. Uncertainties were minimized by measuring a sufficient number of grains, (>500; Lentz and McSween 2000). Kile et al. (2000) selected 300 crystals to measure, but did not have the issue of unknown cuts through the crystals. Bin size was calculated to be one fifth the average core diameter as per the methods of Kile et al. (2000). Histograms for all measurements were graphed, and log-graphed, for each sample and compared to generalized CSDs developed by Eberl et al. (1998). Log-graphs of cumulative histograms have been used to interpret igneous systems (Marsh 1988). This method was applied to MT core size measurements to further examine MT core genesis.

***SIMS Trace Element Imaging***

SIMS (secondary ion mass spectrometry) was used to determine trace element partitioning within MT void-filling microspar. One thick-section from each location (China, Mauritania, Montana, and two Russian locations) was cut to fit a 2.5 cm cartridge, mounted with epoxy, and ground to a high polish. Samples were gold coated to enhance conductivity. Preliminary ion imaging of $^{24}Mg^{2+}$, $^{54}Fe^{2+}$, $^{88}Sr^{2+}$ and $^{55}Mn^{2+}$ was collected for only the Russian sample. Rastered areas of 100µm x 100µm were counted for 200 seconds, with a spatial resolution of 2µm. A primary 0.001 nA beam of $^{16}O^{-}$ ions was used with 4500V secondary ion acceleration. Internal pressure of sample area was $5.5 \times 10^{-9}$ torr, and internal primary column pressure was $5.8 \times 10^{-8}$ torr. Analyses were performed using the Cameca 4f Secondary Ion Mass Spectrometer at Oak Ridge National Lab, Oak Ridge, Tennessee.

***Raman Spectroscopy***

Raman spectroscopy was used to define the current mineral content and to investigate the structure of MT microspar. Raman spectra were acquired in the backscattering mode on the "microstage" of a Labspec Raman spectrometer with a computerized data acquisition system. The microstage uses confocal optics. Both the excitation and the emission radiation pass through the lens nearest the sample. Under the focal and alignment conditions used, this resulted in an excitation beam diameter of ~3 μm at the sample. The monochromator employed an 1800 grooves/mm grating with 200 μm slits, giving a band-pass of 0.5 nm. A holographic notch filter blocking 514 ± 4 nm light was used at the entrance of the monochromator to eliminate elastically scattered laser radiation, protecting the EG&G OMA 4 charge-coupled device detector. Signal to noise ratio was further improved by thermoelectrically cooling the detector to -70°C. The 632.81 nm line of a Coherent Innova 200 He/Ne laser was used for excitation. The laser output power was 8.4 mW when measured at the sample position. Spectra were acquired for 15s over the range of ~150-2000 $cm^{-1}$. Acquisitions were acquired over a 50 $\mu m^2$ area in 3 μm intervals. The spectra were smoothed with a 5-point Savitsky-Golay smooth function. All analyses were conducted in the Chemistry Department at the University of Tennessee, Knoxville.

Differences in mineral content and crystal structure between cores and overgrowths should be reflected in differences in Raman half-widths and spectral peaks respectively. Densities of MT features were measured using standard point counting methods in an attempt to correlate observed spectral features to cores or rims. A grid of 2 μm spots (18 spots x 18 spots = 324 total spots), spaced 3 μm apart, was used to simulate the rastered pattern of Raman measurements during point counting. Densities were compared to observed measurements to determine if distinct features could be resolved.

## V. RESULTS AND INTERPRETATION

### *Elemental and Isotopic Analysis*

Results of elemental analyses (Table 1) show that bulk MT microspar (cores and rims) is a low-Mg calcite within a matrix of more Mg-rich calcite. Mn is an expected trace element as indicated by cathodoluminescence and is always enriched in the matrix relative to the MT void-filling microspar. The highest amount of Mn present is 239 ppm. Fe as is also consistently found in higher concentrations in the surrounding matrix. By contrast, Sr concentrations are consistently higher in MT microspar than in matrix components. Carbon isotope values of the matrix (Table 2) are slightly enriched in $^{13}C$ relative to MT fill, although all carbon and oxygen isotope values are comparable to values projected for coeval Mesoproterozoic seawater (c.f. Kah et al. 1999).

Carbonate rocks typically contain increased concentrations of Mn and Fe and decreased concentration of Sr with increasing diagenetic fluid interaction (Banner and Hanson 1990). Relative to the surrounding matrix, MT microspar contains lower amounts of Mn and Fe, with higher amounts of Sr, and therefore appears less diagenetically altered than the host matrix (Fig. 8). Similarity in both C and O isotopic values between bulk MT microspar and the surrounding matrix (Table 2) suggest preservation of near coeval seawater values.

### *Crystal Size Distributions*

Eberl et al. (1998) first simulated crystal growth with a numerical method that predicts the shapes of CSDs produced from a variety of crystal nucleation and growth scenarios. Three basic shapes of CSDs were produced: asymptotic, lognormal, and a universal steady state shape (Fig. 9). Asymptotic CSDs represent continuous nucleation and growth in an open system in which nucleation occurs at either a constant or accelerating rate. Lognormal CSDs result from surface-controlled growth in an open system, during which crystals grow with an essentially unlimited supply of nutrients. The universal steady state CSD occurs when supply- or surface-

Table 1.-Elemental composition of MT microspar and host rocks

| Sample | Ca (ppm) | Mg (ppm) | Mg/Ca | Mn (ppm) | Fe (ppm) | Sr (ppm) |
|---|---|---|---|---|---|---|
| Mauritania | 338240 | 32361 | 0.10 | 653 | 20314 | 113 |
| Mauritania MT | 397250 | 457 | 0.00 | 203 | 1780 | 210 |
| Russia | 255186 | 96617 | 0.38 | 1055 | 14109 | 111 |
| Russia MT | 398668 | 668 | 0.00 | 239 | 73 | 206 |
| China | 339194 | 46723 | 0.14 | 73 | 1650 | 380 |
| China MT | 384355 | 12036 | 0.03 | 37 | 190 | 658 |

Table 2.- Isotopic composition of MT microspar and host rock

| Sample | $\delta^{13}C$ (‰, VPDB) | $\delta^{18}O$ (‰, VPDB) |
|---|---|---|
| Mauritania | 2.21 | -8.14 |
| Mauritania MT | 2.19 | -11.09 |
| Russia | -0.94 | -8.24 |
| Russia MT | -1.73 | -8.72 |
| China | 3.57 | -8.16 |
| China MT | 3.06 | -6.70 |

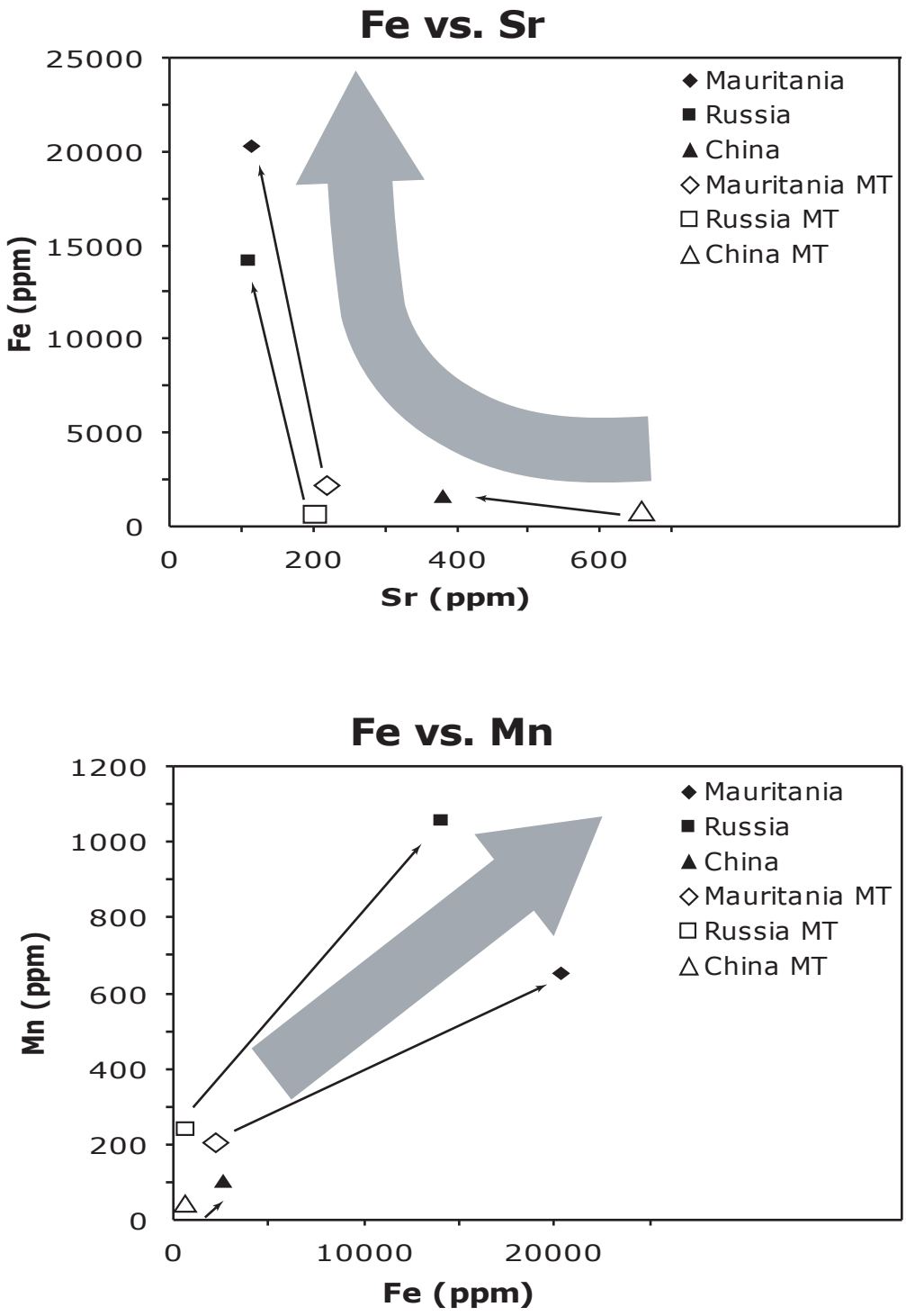


Fig. 8- Elemental composition of MT microspar and host rock. MT microspar is characterized by lower Mn and Fe, and higher Sr concentrations than the surrounding matrix. Gray arrows indicate trends to greater diagenesis indicating that MT microspar is less altered than the host substrate.

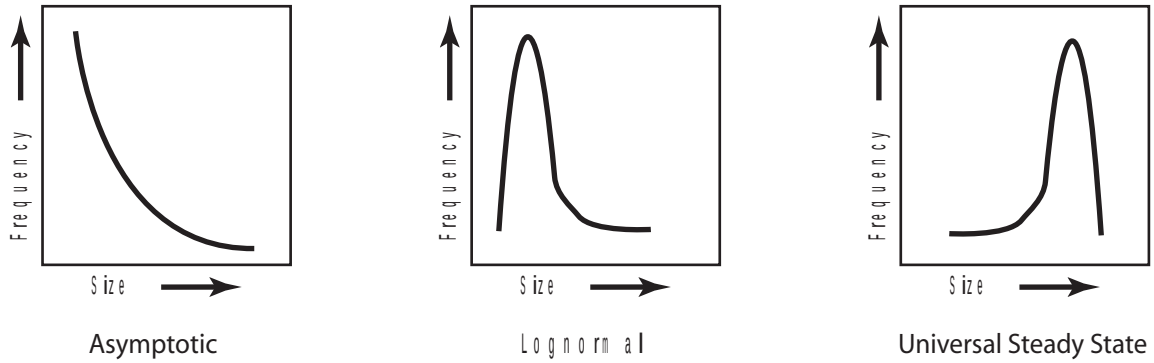


Fig. 9-Theoretical CSD shapes adapted from Eberl et al. (1998). Asymptotic CSDs represent continuous nucleation and growth in an open system in which nucleation occurs at either a constant or accelerating rate. Lognormal CSDs result from surface-controlled growth in an open system, during which crystals grow with an essentially unlimited supply of nutrients. The universal steady state CSD occurs when supply- or surface-controlled Ostwald ripening in a closed system governs crystal growth

controlled Ostwald ripening in a closed system governs crystal growth. In this scenario, crystals dissolve and grow at a rate controlled by differences in specific surface area and by diffusion rate. Intermediate curves (Kile et al. 2000) were interpreted to indicate that crystals formed as a spontaneous event at the nanometer scale, followed by Ostwald ripening which may be related to the degree of carbonate saturation of the precipitating fluids. Nucleation, surface-controlled LPE (Law of Proportionate Effect) growth, and Ostwald ripening occur only at the nanometer scale. However, supply-controlled growth, the period when most of the mass of the crystal is added, dictates that the relative shapes and variances of the CSDs, formed at small sizes, are maintained since crystals grow at the same proportional rate (Kile et al., 2000; Eberl et al, 1998).

CSD shapes of MT microspar (Fig. 10) are uniformly intermediate between lognormal and universal steady state/Ostwald ripening curves predicted by Eberl et al (1998). Kile et al. (2000) produced similar intermediate CSDs for synthetic crystals that precipitated while varying the initial levels of supersaturation. Kile et al. (2000) suggested that these shapes represent systems that have experienced differing degrees of Ostwald ripening, and required rapid nucleation kinetics. Similarity between the Kile et al. (2000) CSDs and MT CSDs suggests that MT microspar cores also formed in a spontaneous nucleation event followed by Ostwald ripening. Supply-controlled growth in supersaturated water controlled the eventual core size.

Standard techniques for interpreting CSDs use log-graphs of the cumulative distribution rather than the distribution itself (Marsh 1988; Cashman and Marsh 1988). MT CSD log-graphs (Fig. 11) show a dominantly negative slope with a turnover in the smallest bin sizes. Linear CSDs with a negative slope suggest conditions of continuous nucleation and growth (Lentz and McSween 2000). However, MT microspar log-graph CSDs are not linear, supporting the idea that MT microspar formed in a spontaneous nucleation event. The turnover at small bin sizes is typical of Ostwald ripening.

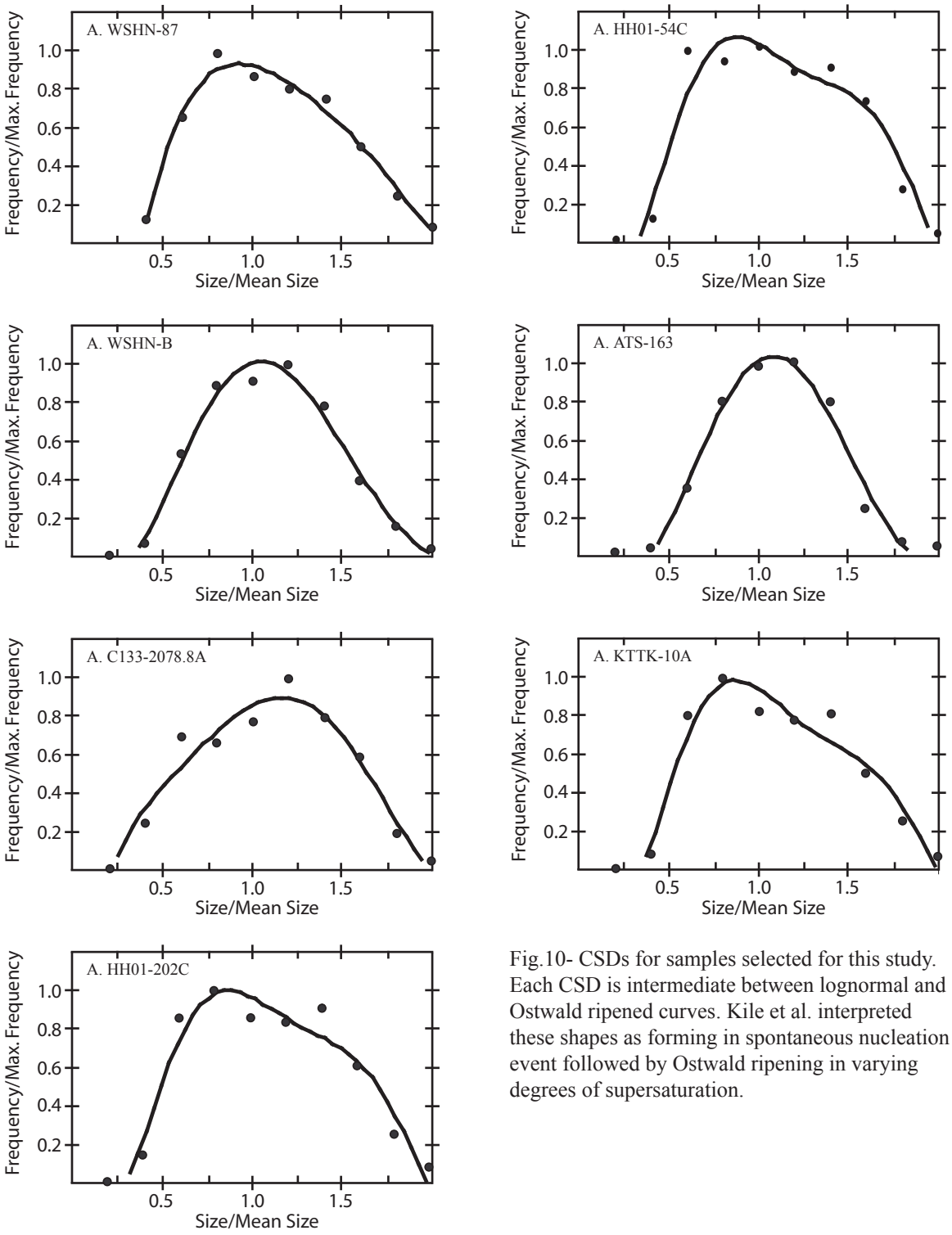


Fig.10- CSDs for samples selected for this study. Each CSD is intermediate between lognormal and Ostwald ripened curves. Kile et al. interpreted these shapes as forming in spontaneous nucleation event followed by Ostwald ripening in varying degrees of supersaturation.

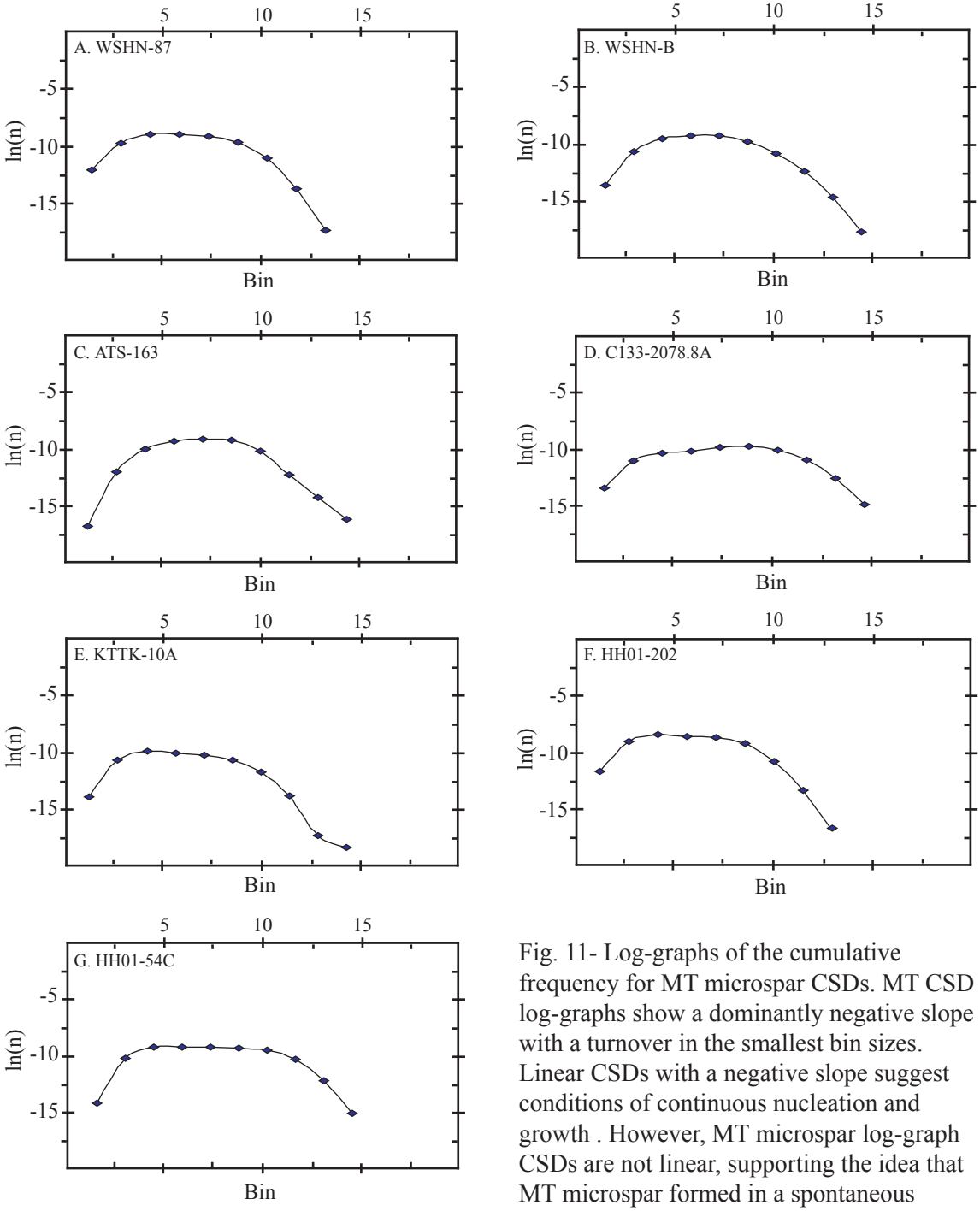


Fig. 11- Log-graphs of the cumulative frequency for MT microspar CSDs. MT CSD log-graphs show a dominantly negative slope with a turnover in the smallest bin sizes. Linear CSDs with a negative slope suggest conditions of continuous nucleation and growth . However, MT microspar log-graph CSDs are not linear, supporting the idea that MT microspar formed in a spontaneous nucleation event. The turnover at small bin sizes is typical of Ostwald ripening. Bin size is 1/5 mean crystal size consistent with methods used by Kile et al. 2000.

In most cases, cores from different locations are of similar size (mean size ranges from 5.6 - 7.7 μm). When segregated based on core shape, round and rhombic cores consistently maintain the mean crystal size and basic CSD shape, as the group as a whole. This suggests that any volume change resulting from potential mineralic transformation has not obscured original nucleation and growth information.

***SIMS Analysis***

One way of determining original minerals of recrystallized samples is to examine trace element incorporation. For example, calcite originating from the recrystallization of aragonite typically has elevated Sr concentrations, because aragonite readily incorporates Sr as a trace element (Holland, 1963; Holland et al. 1964; Kinsman and Holland, 1969; Malone and Baker, 1999). Similarly, Mn and Fe are more commonly substituted into dolomite because of their smaller ionic radius.

SIMS ion mapping provides qualitative data regarding trace element incorporation into the crystal structure of MT microspar. Figure 12 shows $^{24}Mg^{2+}$, $^{54}Fe^{2+}$, $^{88}Sr^{2+}$ and $^{55}Mn^{2+}$ ion maps. Images were enhanced with color to reveal contrast. $^{88}Sr^{2+}$ (Fig. 12a) and $^{54}Fe^{2+}$ (Fig. 12b) in MT microspar is nearly undetectable. Low $^{88}Sr^{2+}$ supports previous elemental data and suggests that an original aragonitic composition for either core or rim precipitates is unlikely. The $^{24}Mg^{2+}$ image (Fig. 12c, 12e) reveals sub-rounded forms with $^{24}Mg^{2+}$ concentrated near the center and becoming more diffuse away from the center. The interpretation is that these sub-rounded forms are the dully luminescent cores of the MT microspar. By contrast, $^{55}Mn^{2+}$ is depleted within the cores, but appears to be enriched outside the cores (Fig.12d, 12e) as predicted from CL analysis. A composite color overlay of the $^{55}Mn^{2+}$ and $^{24}Mg^{2+}$ images, with colors randomly assigned to each element is shown in Fig. 12e. This composite image shows features similar to those of the CL images of MT microspar.

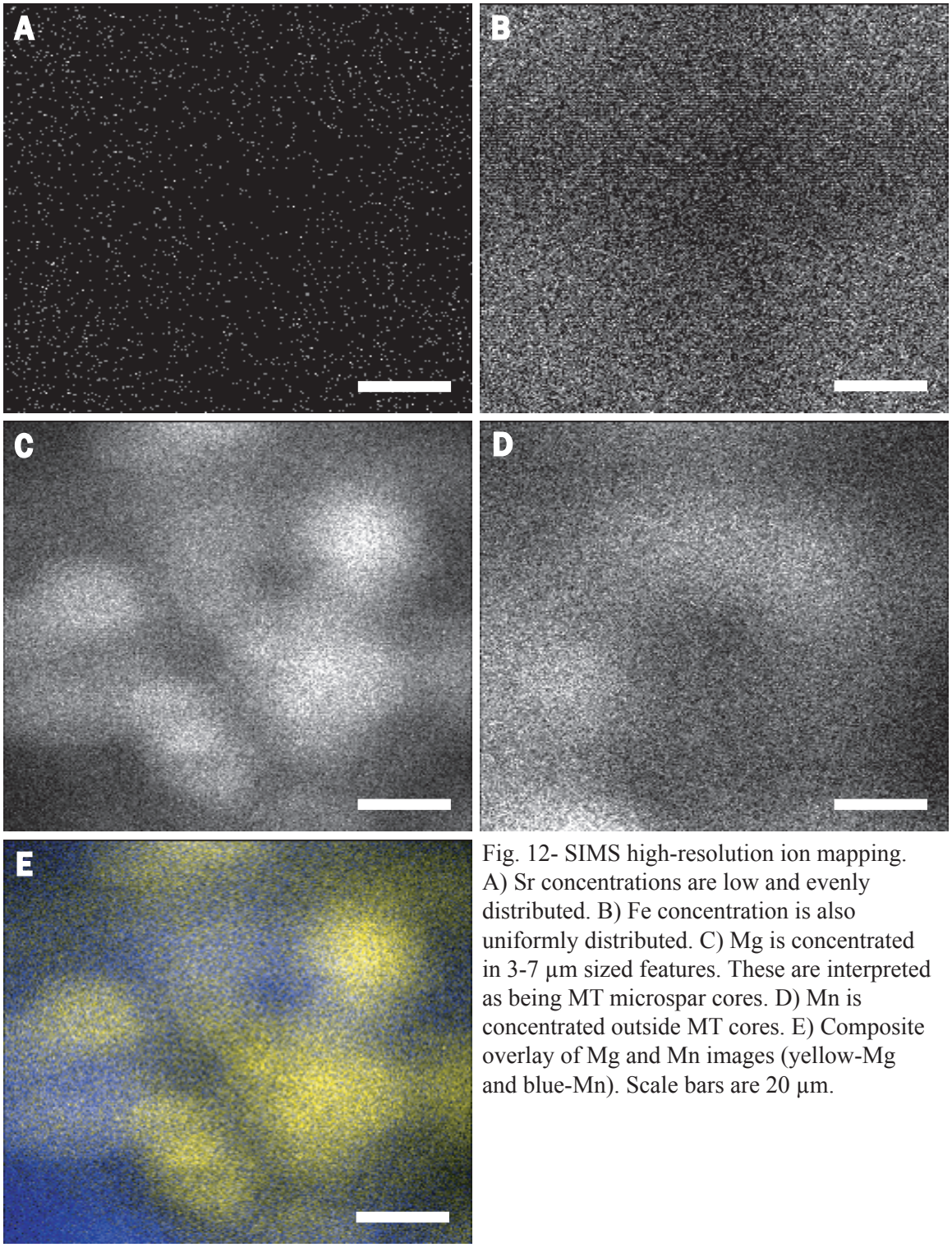


Fig. 12- SIMS high-resolution ion mapping. A) Sr concentrations are low and evenly distributed. B) Fe concentration is also uniformly distributed. C) Mg is concentrated in 3-7 µm sized features. These are interpreted as being MT microspar cores. D) Mn is concentrated outside MT cores. E) Composite overlay of Mg and Mn images (yellow-Mg and blue-Mn). Scale bars are 20 µm.

Interestingly, SIMS imaging suggests a decrease in $Mg^{2+}$ concentration from the center of the cores outward. This observation leads to three hypotheses: 1) the fluid source became progressively depleted in $Mg^{2+}$ during precipitation as the $Mg^{2+}$ became sequestered in the nucleus of the cores, 2) $Mg^{2+}$ was originally incorporated uniformly throughout the cores, but $Mg^{2+}$ was expelled from the system during diagenesis or recrystallization, or 3) $Mg^{2+}$ concentrations reflect growth rate dependent $Mg^{2+}$ substitution, wherein $Mg^{2+}$ substitution is greater during initial crystallization.

The first hypothesis, progressive depletion of $Mg^{2+}$ in source fluids, seems unlikely. In Mg-rich fluids, $Mg^{2+}$ concentration would be expected to remain basically unchanged during crystal precipitation because only trace amounts of $Mg^{2+}$ are typically incorporated into the calcium carbonate crystal structure. The precipitating fluid would thus remain Mg-rich and incorporation of $Mg^{2+}$ into precipitating minerals would not be supply-controlled. The second hypothesis, diffusion of $Mg^{2+}$ out of cores during diagenesis, also seems unlikely. Petrographic evidence suggests that polygonal rim cements formed early prior to compaction of sedimentary matrix. This is evidenced by the absence of clastic sediment in-filling MT cracks, and by soft-sediment deformation around the already rigid crack. Uniform distribution of various MT core morphologies coupled with overgrowth cements of equal thickness suggests that if cores formed by spontaneous nucleation, cements preserve core shapes representing various stages of transformation. Hypothesis three, growth rate dependent $Mg^{2+}$ substitution seems most likely. In one scenario, factors such as the presence of dissolved organic molecules or elevated carbonate saturations affect the rate of calcium carbonate formation (Kitano 1965; Kitamura 2002). It is possible that, as precipitation continued, growth slowed, resulting in a decrease in $Mg^{2+}$ incorporation.

$Mn^{2+}$ ion imaging supports observations made under cathodoluminescence, with highest concentrations observed outside the MT cores. Pollock et al. (2006) suggested that MT structures

formed in association with decaying OM in the presence of oxygen. This oxygen may have also oxidized nucleation–growth inhibitors (e.g. $Fe^{2+}$ and $Mn^{2+}$), limiting incorporation into MT cores. However, these processes may have utilized the oxygen in the immediate system, allowing incorporation of $Fe^{2+}$ and $Mn^{2+}$ into the overgrowth cements as primary features. Pope et al. (2003) suggested that rapid MT precipitation occurred in a supersaturated environment with a sharply declining oxygen gradient in the sediment and low oxygen levels in contemporaneous seawater. This may explain the partitioning of $Mn^{2+}$ in MT microspar overgrowths.

***Raman Spectroscopy***

The petrographic relationships between core morphologies, and the presence of CL luminescent banding suggest that spheroidal MT cores were unstable, and underwent transformation to rhombic shape. The preservation of spheroidal core morphologies, however, suggests that some remnants of previous initial mineralogy may still remain. Micro-Raman spectroscopy is an ideal way to identify the mineralogical variation between current MT cores and rims as well as the presence of lattice defects resulting from mineralogical transformation. Raman spectroscopy is the measurement of the wavelength and intensity of inelastically scattered light from molecules. The Raman scattered light occurs at wavelengths that are shifted from the incident light by the energies of molecular vibrations, related to the architecture of the crystal's unit cell. $CaCO_3$ polymorphs have distinct and well known Raman spectra (Bischoff et al., 1985; Urmos et al., 1991; Gauldie et al., 1997) Similarly, half-widths (the full width of Raman bands at half the maximum band height) of Raman spectra are known to vary with crystallinity of the sample (i.e. presence of structural defects and crystallite size) and substitution of trace elements (Bischoff et al., 1985). For instance, as $Mg^{2+}$ concentrations in carbonates increase, halfwidths of the internal modes also increase. Because $CaCO_3$ polymorphs have different structures, they likely possess different trace element chemistry (Gauldie et al., 1997; Kahmi, 1963) that might be

recorded in the Raman spectra. Furthermore, spectra can be measured in spatial increments of 1-5 μm making it possible to spatially distinguish cores from rims.

If originally precipitated as a mineralogically unstable form, all cores regardless of shape are likely to have transformed to current calcitic composition. Rhombic cores represent recrystallized forms are expected to reveal Raman spectra typical of calcite. Conversely, round cores that represent initial crystal forms "entrapped" by cement prior to transformation, might reveal lattice disruption related to transformation with volume and morphology retention, and should show a slight increase in half-width of Raman spectra which arises from positional disorder of carbonate ion resulting from rotation of the $CO_3^{2-}$ out of the basal plane (Bischoff et al., 1985).

Calcite (particularly low-Mg calcite) has two low frequency lattice modes (Table 3), one related to translational (t) oscillations and one related to librational (l) oscillations. These two modes are related to the rhombohedral unit cell of. Additional higher frequency vibrational (v) modes also occur: v1 is associated with symmetric stretch, v2 with out-of-plane bending, v3 with anti-symmetric stretch, and v4 with in-plane bending of $CO_3^{2-}$ (Gauldie et al., 1997). With increasing Mg concentration, calcite spectral peaks shift to higher frequencies (Bischoff 1985). Other polymorphs of $CaCO_3$, aragonite (orthorhombic) and vaterite (hexagonal), have 9 and 8 lattice modes respectively (Table 3). These result from the larger number of formula units in their unit cells. Splitting of the v3 peak is common in both aragonite and vaterite, and splitting of the v4 and 2xv2 peaks is common in vaterite.

Raman spectra from all MT samples were collected over a 50 $\mu m^2$ area in 3μm increments giving 324 spectra per sample (representative spectra shown in Fig.13). Spot size was constrained to 2 μm to ensure that measurements could be collected from entirely within MT cores. In each sample, spectral peak position lacked variance except within the error of the

Table 3.- Measured spectral peaks of different calcium carbonate polymorphs.

| Polymorph[1] | Lattice Modes | v4 | v1 | v3 | 2x v2 |
|---|---|---|---|---|---|
| Calcite | 154, 281 | 711 | 1085 | 1434 | 1748 |
| 8.0% Mg Calcite | 156, 284 | 714 | 1087 | 1438 | 1749 |
| Aragonite | 113, 142, 153, 180, 190, 206, 242, 261, 284 | 1085 | - | 1462/1574 | 701 |
| Vaterite | 106, 116, 150, 177, 210, 268, 301, 330 | 1066/1093 | 845 | 1416/1466 | 713/752 |

[1]calcite data from Bischoff et al. (1985), synthetic aragonite and vaterite data from Gauldie et al. (1997).

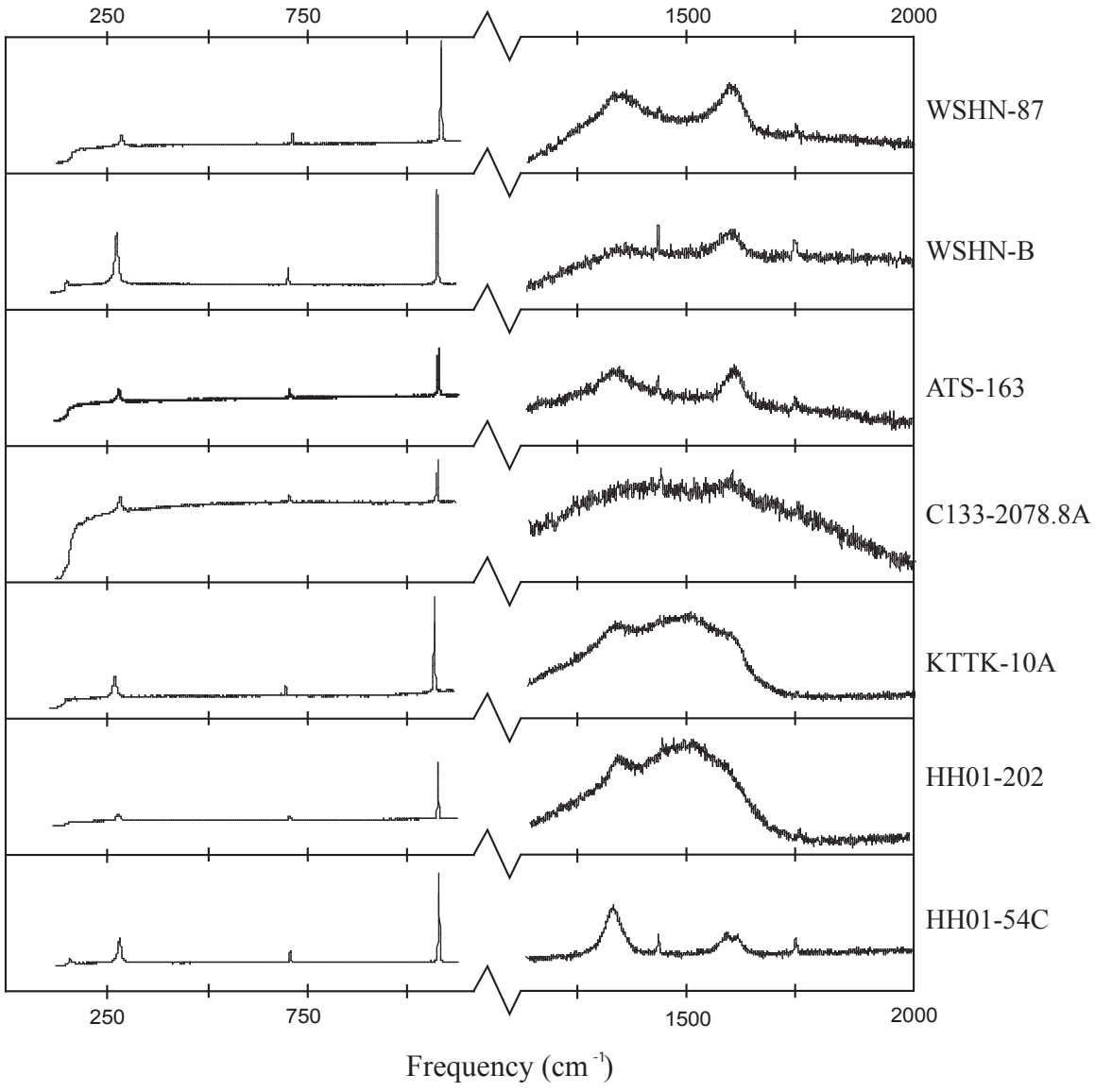


Fig. 13- Typical Raman spectrum for each sample. Y-axis is non-calibrated intensities. Peaks located at 1087 have been truncated for legibility. Spectral peaks from ~1150-2000 have been enhanced to compensate for low intensities. Fluorescence features occur at ~156, 1336 and 1600.

machine. MT microspar consistently showed five peaks located at approximately 158 $cm^{-1}$, 283 $cm^{-1}$, 714 $cm^{-1}$, 1087 $cm^{-1}$, 1436 $cm^{-1}$, and 1749 $cm^{-1}$. No splitting of peaks is observed in MT microspar.

MT microspar spectral peaks (number and frequency) are consistent with spectral peaks of low-Mg calcite. However, some anomalous weak peaks (179 $cm^{-1}$, 200 $cm^{-1}$, and 223 $cm^{-1}$) occur in the range of lattice modes for $CaCO_3$ polymorphs. It is possible that these peaks represent remnants of a previously unstable mineral and current structural disorder associated with transformation. When compared with spectra of $CaCO_3$ polymorphs, peak 179 is similar to a known peak for vaterite, but peaks 200 and 223 are dissimilar to peaks of either polymorph. Since lattice mode spectral peaks are associated with the number of molecules in the crystal lattice, it is possible that these peaks represent a crystal lattice construction modified from the known $CaCO_3$ polymorphs.

Bischoff et al. (1985) measured the half-widths of spectral peaks associated with the calcite lattice and its vibrational modes and noted that half-widths increased with increasing Mg content of calcite and associated increased structural disorder. MT microspar half-widths (Table 4) typically fall in a range that is consistent with low Mg-calcite. These half-width data suggest that no remnant instability remains, except for that associated with Mg incorporation. Groupings of measured half-widths show no correlation to density of MT cores, so distinction of core to overgrowth is not possible with our Raman data. It is possible that half-widths are affected by incorporation of transition metal cations other than Mg. In MT microspar, Mn in overgrowths could affect half-widths similarly as Mg affects MT cores. Some samples had 2xv2 peaks with wider half-widths than those expected of low-Mg calcite. These inconsistencies may result from strain associated with lattice disorder resulting from mineralogical transformation.

Table 4- Observed half-widths of Mg-calcites (from Bischoff 1985) and MT microspar samples.

| Sample | T [1] | L [2] | v4 [3] | v1 [4] | v3 [5] | 2x v2 [6] |
|---|---|---|---|---|---|---|
| Calcite | 6.2 | 10.1 | 3.6 | 2.5 | 2 | 3.6 |
| 1.9% Mg-Calcite | 8.2 | 12.0 | 4.8 | 4.2 | 6.4 | 7.6 |
| 3.9% Mg-Calcite | 10.7 | 13.8 | 5.9 | 5.6 | 7.6 | 8.3 |
| 5.7% Mg-Calcite | 11.5 | 15.6 | 7.4 | 6.5 | 10.2 | 9.5 |
| 8.0% Mg-Calcite | 13.3 | 15.1 | 8.7 | 7.1 | 11.4 | 9.5 |
| 9.9% Mg-Calcite | 14.7 | 18.3 | 9.7 | 7.6 | 14 | 10.8 |
| 12.5% Mg-Calcite | 15.9 | 20.0 | 12.2 | 9.2 | 17.8 | 11.5 |
| 15% Mg-Calcite | im [7] | 18.3 | 12.2 | 8.6 | 19.1 | 11.5 |
| | | | | | | |
| MT WSHN-87 | im | 9.13-12.18 | 3.04-5.07 | 3.04-4.06 | 1.74-8.71 | 1.74-10.45 |
| MT WSHN-B | im | 10.15-12.18 | 4.06-5.08 | 4.06 | 1.74-6.97 | 1.74-10.45 |
| MT ATS-163 | im | 8.12-12.18 | 4.06-5.08 | 3.04-4.06 | 1.74-7.84 | 1.74-10.45 |
| MT C133-2078.8A [8] | im | 8.12-12.18 | 3.04-6.09 | 3.04-4.06 | 1.74-6.97 | 1.74-6.1 |
| MT KTTK-10A [8] | im | 9.13-13.19 | 4.06-6.09 | 3.04-5.08 | 1.74-14.81 | 1.74-6.1 |
| MT HH01-202 [8] | im | 10.15-13.19 | 3.04-6.09 | 3.04-5.08 | 1.74-12.19 | 1.74-9.58 |
| MT HH01-54C | im | 8.12-13.19 | 4.06-6.09 | 3.04-5.07 | 1.74-7.84 | 2.61-10.45 |

[1] Vibration related to doubly degenerate translation
[2] Vibration related to doubly degenerate libration
[3] Vibration related to in-plane bend
[4] Vibration related to symmetric stretch
[5] Vibration related to Antisymmetric stretch
[6] Second-order Raman band is an overtone of the infrared-active mode
[7] Immeasurable
[8] Strong fluoresence makes v3 and 2xv2 peaks obscured

Fluorescence often occurs in calcite because of trace amount of transition metal ions incorporated into the crystal lattice. This fluorescence interferes particularly with the low frequency translation mode at 158 $cm^{-1}$, making a baseline correction difficult. Fluorescence at ~1330 $cm^{-1}$ and ~1600 $cm^{-1}$, typical in calcite (Bischoff 1985), also occur in MT microspar. This was coupled with low signal to noise ratios and made some of the v3 and 2xv2 peaks immeasurable.

Combined, these observations suggest that MT microspar (both cores and overgrowths) are currently low Mg-calcite. SIMS ion imaging shows preferential Mg incorporation unto MT cores, which likely accounts for the breadth of peak half-widths. Several anomalous, weak–intensity, low frequency peaks may indicate disorder in the current crystal structure.

## VI. DISCUSSION

### *Model for MT Microspar*

Observations and analyses of this study allow expansion on previously hypothesized models of MT formation. Only the gas-escape model (Furniss et al. 1998; Pollock et al. 2006) accounts for both the various shapes of MT structures and their early post-depositional formation near the sediment-water interface. In this hypothesis, gases form in the shallow sub-surface by the decay of organic matter (Furniss et al. 1998; Pollock et al. 2006), or by clathrate destabilization (Marshall and Anglin 2004). These gases propogate through the sediment forming variously shaped voids, and substrate cohesion ultimately controls the morphology of these voids. Supersaturated pore fluids then migrate into the voids immediately after gas migration, triggering spontaneous nucleation and precipitation of void-filling cement (Pollock 2006).

MT microspar consists of equant, non-interlocking crystals whose rounded shape and uniform crystal size (ranging in diameter from 7-15 μm), suggest that they might have been precipitated as vaterite (Gellatly 1999). Vaterite (Fig 14) is a highly unstable polymorph of $CaCO_3$ that precipitates as homogeneously nucleated, sub-spherical crystals under highly supersaturated laboratory conditions and converts rapidly to calcite (Kralj et al., 1990). Cathodoluminescence of MT cements reveals poorly luminescent, sub-spherical to rhombic cores surrounded by a more luminescent, polygonal cement rim. Preservation of these sub-spherical crystals suggests that early lithification by rim cements may have helped preserve the primary crystal morphology associated with original vaterite precipitation. Spheroidal vaterite precipitation has been linked to the presence of dissolved organic molecules which act as nucleation sites. If the sediment water interface is sealed with microbial mats, decaying OM would be abundant within the underlying soft sediment. Any gas formed in the substrate would escape in random patterns leaving behind voids in the soft sediment (c.f. gas escape model

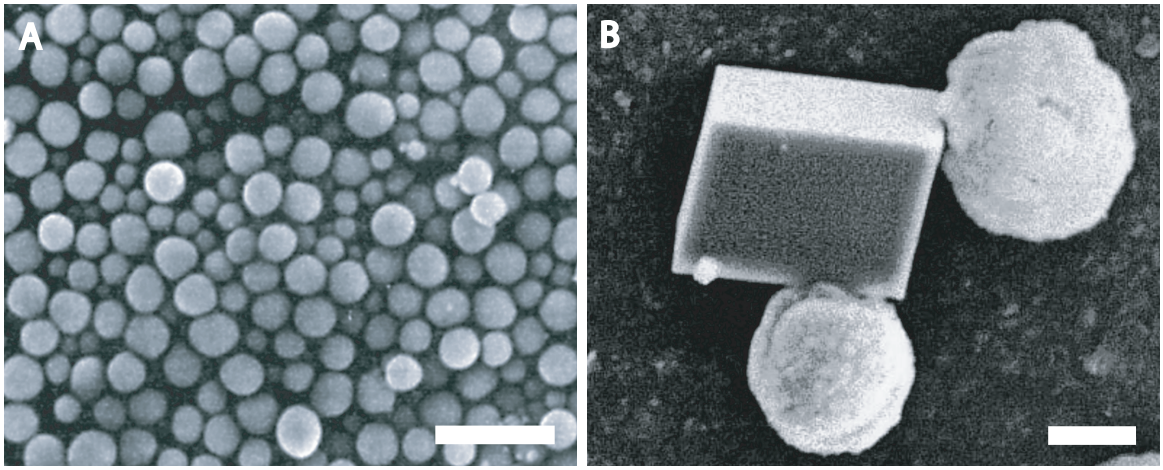

Fig. 14- SEM images of vaterite. A) SEM image of spheroidal vaterite from Naka et al. 2002. B) SEM image reveals spheroidal vaterite and rhombic calcite transformed from spheroidal vaterite (Hobbs and Reardon 1999). Scale bars for A and B are 15 and 3 μm respectively.

Furniss, 1998 and Pollock et al. 2006). Supersaturated Precambrian ocean waters migrating into voids would transport abundant OM into those voids. Together, supersaturated pore-waters and dissolved OM would facilitate vaterite precipitation. Ultimately these vateritic "cores" would act as nucleation sites for the overgrowth cements, preserving the MT voids.

***Implications of Analysis***

Transmitted light microscopy reveals polygonal carbonate crystals, with non-interlocking, sharp crystal boundaries, that contain no cloudiness related to neomorphic recrystallization, suggesting primary precipitation, not neomorphism. MT microspar's sharp contact with the surrounding sediment suggests that indeed MT structures were previously voids. Cathodoluminescence reveals that MT microspar crystals are two phase: 1) variously shaped cores 2) with polygonal overgrowths. Typically, MT microspar has dominantly spheroidal cores (3-12 μm), consistent with a vaterite precursor. Void formation, core nucleation and growth, and overgrowth formation, must have occurred rapidly, essentially synsedimentary. Similarly, vaterite formation is often associated with rapid nucleation and growth (Sawada 1990).

CSDs of the MT microspar cores reveal that crystals originally nucleated in a spontaneous event followed by a period of Ostwald ripening. Rapid supply-controlled growth in supersaturated ocean waters allowed cores to fill MT voids, preserving MT void morphologies. Elemental analysis indicates that MT microspar is less altered than the surrounding matrix, suggesting primary chemistry is preserved. If MT microspar originally precipitated as vaterite, isotopically light carbon values might be expected from decaying OM influencing nucleation. Although isotopic analysis indicates near zero carbon values, negative carbon values associated with organic matter may be obscured by global ocean carbon buffering (Bartley and Kah 2004), because dissolved inorganic carbon (DIC) reservoir may have been up to 10x that of today. This

elevated DIC may buffer fluid composition even in the presence of isotopically light organic carbon (e.g. decaying organic matter).

SIMS ion mapping shows that MT cores are enriched in $^{24}Mg^{2+}$. Although relatively little is known about trace element incorporation into vaterite, precipitation experiments have placed some constraints on the relationship between $Mg^{2+}$ and $CaCO_3$ polymorph formation (Sawada, 1990; Kitano, 1962). Elevated concentrations of $Mg^{2+}$ have been suggested to favor aragonite formation when precipitation rate is slow (Kitano, 1962). However, recent experiments suggest that when precipitation occurs rapidly, elevated concentrations of $Mg^{2+}$ favor vaterite nucleation (Sawada, 1990). The distribution coefficient of $Mg^{2+}$ ($D_{Mg}$) for vaterite is typically higher than that for calcite (Table 5). If MT microspar originally precipitated as vaterite, high levels of $Mg^{2+}$ might be expected within the *rounded* cores, even after neomorphic recrystallization, relative to the polygonal overgrowths. *Rhombic* cores, presumably undergoing calcite-vaterite transformation prior to overgrowth cements, should have less Mg than round cores because Mg should have been released into ambient fluids from the crystal during mineralogical transformation. However, ion imaging reveals no distinction between round and rhombic cores. Progressive decrease in Mg from core to rim is revealed in the Mg ion image. In lab experiments, supersaturation of $Ca^{2+}$ and $CO_3^{2-}$ lead to high vaterite nucleation rates (Kitamura, 2002). Possibly, as carbonate saturation decreases during crystal growth from a semi-closed system (i.e. sealed microbial mats), rate of growth slows, resulting in lower $Mg^{2+}$ incorporation.

The unstable nature of vaterite would suggest that if MT microspar was originally precipitated as vaterite, it should have quickly converted to calcite. The preservation of spheroidal core morphologies suggests that some remnants of previous vaterite mineralogy may still remain. All cores regardless of shape should have transformed to calcite. We expected that rhombic cores might represent vaterite that underwent vaterite-calcite transformation prior to cement overgrowths, and might have Raman spectra typical of calcite.

Table 5-Distribution coefficient of Mg for various phases.

| $C_{Ca}$ (M) | $C_{Mg}$ (M) | $D_{Mg}$ Vaterite | $D_{Mg}$ Calcite[a] | $D_{Mg}$ Calcite[b] |
|---|---|---|---|---|
| 0.01 | 0.01 | 0 | 0 | 0.031 |
| 0.01 | 0.001 | 0.042 | 0 | 0.036 |
| 0.01 | 0.0001 | 0.048 | 0.02 | 0.055 |
| 0.001 | 0.001 | 0.073 | 0.012 | 0.049 |
| 0.001 | 0.0001 | 0.083 | 0.018 | 0.071 |

a) calcite slowly formed from vaterite transformation

b) calcite rapidly formed from amorphous $CaCO_3$

Conversely, spheroidal cores represent vaterite that was entrapped by cement prior to transformation. Spheroidal cores might have structural disorder related to recrystallization with morphology and volume retention and show a slight increase in halfwidth of Raman spectra arising from positional disorder of carbonate ion (Bischoff et al., 1985). Frequencies of Raman spectra of MT microspar are consistent with low Mg-calcite. Since MT microspar is a low-Mg calcite, anomalous low-frequency Raman peaks, coupled with occasional wide high frequency peaks, suggest additional instability that is not associated with Mg incorporation. Both aragonite and vaterite have numerous low frequency lattice modes, which is associated with the large number of formula units in their unit cell. Additional lattice mode peaks in MT microspar may result from the spheroidal vateritic cores incompletely transforming to the proper unit cell of calcite.

## VII. CONCLUSION

Petrographic evidence suggests that MT microspar is an unusual form of primary calcium carbonate precipitate that may be linked to decaying OM (Pollock et al. 2006). The spheroidal cores of the two-part MT microspar crystals are morphologically similar to spheroidal vaterite. CSDs of MT cores show that nucleation and growth history is also consistent with vaterite precipitation. The ion images from the secondary ion mass spectrometer indicate that the rounded cores of molar-tooth microspar are enriched in $Mg^{2+}$ at their cores with decreasing concentrations near the rim relative to the polygonal overgrowths. The $Mg^{2+}$ ion images considered with three main lines of background information (1. Mg plays a role in vaterite precipitation, 2. $Mg^{2+}$ substitutes into the vaterite crystal lattice easily relative to calcite, and 3. CL and elemental data indicate that the MT cores have been little affected by diagenesis) lead to the preliminary conclusion that MT microspar cores originally precipitated as vaterite. Raman spectroscopy of MT microspar indicates that the current mineralogy is low Mg-calcite. Anomalous features in Raman spectra may indicate current lattice disorder associated with vaterite-calcite transformation.

## REFERENCES

Abegg, F., Anderson, A.L., 1997, The acoustic turbid layer in muddy sediments of the Eckernfoerde Bay, Western Baltic: methane concentration, saturation and bubble characteristics: Marine Geology, v. 137, p. 137-147.

Banner, J.L., Hanson, G.N., 1990, Calculation of simultaneous isotopic and trace element variations during water-rock interaction with applications to carbonate diagenesis: Geochemica et Cosmochemica Acta, V. 54, p. 3123-3137.

Bartley, J.K., Kah, L.C., 2004,Marine carbon reservoir, $C_{org}$-$C_{carb}$ coupling, and the Proterozoic carbon isotope record: Geology, v. 32, p. 129-132.

Bartley, J.K., 1996, Actualistic taphonomy of cyanobacteria: implications for the Precambrian fossil record: Palaios, v. 11, p. 571-586.

Bauermann, H., 1885, Report on the geology of country near the forty-ninth parallel of the north latitude west of the Rocky Mountains: Canadian Geological Survey, Report of Progress 1882-84, pt. B, p. 1-42.

Bell, R.T., 1966, Precambrian rocks of the Tuchodi Lakes map-area, northeastern British Columbia, Canada [unpublished Ph.D. thesis]: Princeton University, p. 138.

Bischoff, W.D., Sharma, S.K., and MacKenzie, F.T., 1985, Carbonate ion disorder in synthetic and biogenic magnesian calcites; a Raman spectral study: American Mineralogist, v. 70, p. 581-589.

Bishop, J.W., Sumner, D.Y., *in revision*, Molar tooth structures of the Neoarchean Monteville Formation, Transvaal Supergroup, South Africa: I. Description and constraints on microspar precipitation: Sedimentology.

Calver, C.R., Ballie, P.W., 1990, Early diagenetic concretions associated with intrastratal shrinkage cracks in an upper Proterozoic dolomite, Tasmania, Australia: Journal of Sedimentary Petrology, v. 60, p. 293-305.

Cashman, K.V., Ferry, J.M., 1988, Crystal size distribution (CSD) in rocks and the kinetics and dynamics of crystallization: Contributions to Mineralogy and Petrology, v. 99, p. 401-415.

Daly, R.A., 1912, Geology of the North American Cordillera at the forty-ninth parallel: Canadian Geological Survey, Memoir 38.

Demicco, R.V., Hardie, L.A., 1994, Sedimentary structures and early diagenetic features of shallow marine carbonate deposits: SEPM Atlas Series, v. 1, p. 68-71.

Eberl, D.D., Drits, V.A., Srodon, J., 1998, Deducing growth mechanisms for minerals from the shapes of crystal size distributions: American Journal of Science, v. 298, p. 499-533.

Eby, D.E., 1977, Sedimentation and early diagenesis within eastern portions of the “Middle Belt Carbonate Interval” (Helena Formation), Belt Supergroup (Precambrian Y), western Montana [unpublished Ph.D. thesis]: State University of New York, Stony Brook, p. 1-712.

Episodes, 2003, Recent advance in Precambrian carbonate sedimentary geology: Report on International Conference of IGCP447 on Molar Tooth Carbonates and Evolution of the Earth in the Proterozoic: International Union of Geological Sciences Conference Report, v. 26, p. 28-29.

Fairchild, I.J., Einsele, G., Song, T., 1997, Possible seismic origin of molar-tooth structures in Neoproterozoic carbonate ramp deposits, north China: Sedimentology, v. 44, p. 611-636.

Frank, T.D., Lyons, T.W., 1998, "Molar-tooth" structures: A geochemical perspective on a Proterozoic enigma: Geology, v. 26, p. 683-686.

Furniss, G., Rittel, J.F., and Winston, D., 1998, Gas bubble and expansion crack origin of "molar-tooth" calcite structures in the Middle Proterozoic Belt Supergroup, western Montana: Journal of Sedimentary Research, v. 68, p. 104-114.

Gauldie, R.W., Sharma, S.K., Volk, E., 1997, Micro-Raman spectral study of vaterite and aragonite otoliths of the Coho salmon, Oncorhynchus kisutch: Comparative Biochemistry and Physiology, v. 118a, p. 753-757.

Gellatly, A.M., Winston, D., 1999, Were "molar-tooth gas expansion voids in the Helena Formation (Middle Proterozoic Belt Supergroup, Montana) initially filled by vaterite?: Abstracts with Programs Geological Society of America v. 31(4), p. 13.

Grotzinger, J.P., 1989, Facies and evolution of Precambrian depositional systems; emergence of the modern platform archetype, in Crevello, P.D., Wilson, J.J., Sarg, J.F., and Read, J.F., eds., Controls on Carbonate Platform and Basin Development: SEPM Special Publication v. 44, p. 79-106.

Grotzinger, J.P., Knoll, A.H., 1999, Stromatolites in Precambrian carbonates: evolutionary mileposts or environmental dipsticks?: Annual Review, Earth and Planetary Science, v. 27, p. 313-358.

Hemming, N.G., Meyers, W.J., Grams, J.C., 1989, Cathodoluminescence in diagenetic calcites: the roles of Fe and Mn as deduced from electron probe and spectrophotometric measurements: Journal of Sedimentary Petrology, v. 59, p. 404-411.

Hofmann, H.J., 1985, The mid-Proterozoic Little Dal macrobiota, Mackenzie Mountains, Northwest Canada: Paleontology, v. 28, p. 331-354.

Holland, H.D., Borcsik, M., Munoz, J.L., Oxburgh, U.M., 1963, The coprecipitation of $Sr^{2+}$ with aragonite and of $Ca^{2+}$ with strontionite between 90 and 100ºC: Geochimica et Cosmochimica Acta, v. 27, p. 957-977.

Holland, H.D., Holland, H.J., Munoz, J.L., 1964, The coprecipitation of cations with $CaCO_3$. II. The coprecipitation of $Sr^{2+}$ with calcite between 90 and 100ºC: Geochimica et Cosmochimica Acta, v. 28, p. 1287-1302.

Horodyski, R.J., 1976, Stromatolites of the Upper Siyeh Limestone (Middle Proterozoic), Belt Supergroup, Glacier National Park, Montana: Precambrian Research, v. 3, p. 517-536.

James, N.P., Narbonne, G.M., Sherman, A.G., 1998, Molar-tooth carbonates: shallow subtidal facies of the mid- to late Proterozoic: Journal of Sedimentary Research, v.68, p. 716-722.

Kah, L.C., Knoll, A.H., 1996, Microbenthic distribution of Proterozoic tidal flats: environmental and taphonomic considerations: Geology, v. 24, p. 79-82.

Kah, L.C., Sherman, A.B., Narbonne, G.M., Kaufman, A.J., Knoll, A.H., 1999, $\delta^{13}C$ stratigraphy of the Proterozoic Bylot Supergroup, northern Baffin Island: Implications for regional lithostratigraphic correlations: Canadian Journal of Earth Sciences, v. 36, p. 313-332.

Kamhi, S.R., 1963, The structure of vaterite, $CaCO_3$ : Acta Crystallographica, v. 16, p. 770-772.

Kile, D.E., Eberl, D.D., Hoch, A.R., and Reddy, M.M., 2000, An assessment of calcite crystal growth mechanisms based on crystal size distributions: Geochimica et Cosmochimica Acta, v. 64, p. 2937-2950.

Kinsman, J.J., Holland, H.D., 1969, The coprecipitation of cations with $CaCO_3$-IV. The coprecipitation of Sr2+ with aragonite between 16º and 96º C: Geochimica et Cosmochimica Acta, v. 33, p. 1-17.

Kitamura, M., 2002, Controlling factor of polymorphism in crystallization process: Journal of Crystal Growth, p. 2205-2214.

Kitano, Y., Park, K., Hood, D.W., 1962, Pure aragonite synthesis: Journal of Geophysical Research, v. 67, p. 4873-4874.

Kitano, Y., Hood, D.W., 1965, The influence of organic material on the polymorphic crystallization of calcium carbonate: Geochimica et Cosmochimica Acta, v. 29, p. 29-41.

Kralj, D., and Brecevi'c, L., 1990, Vaterite growth and dissolution in aqueous solution I; kinetics of crystal growth: Journal of Crystal Growth, v. 104, p. 793-800.

Knoll, A.H., Swett, K., 1990, Carbonate deposition during the Late Proterozoic era: an example from Spitzburgen: American Journal of Science, v. 290-A, p. 104-132.

Lentz, R.C., McSween, H.Y., 2000, Crystallization of the basaltic shergottites: Insights from crystal size distribution (CSD) analysis of pyroxenes: Meteorites and Planetary Science, v. 35, p. 919-927.

Malone, M.J., Baker, P.A., 1999, Temperature dependence of the strontium distribution coefficient in calcite; an experimental study from 408 degrees to 2008 degrees C and application to natural diagenetic calcites: Journal of Sedimentary Research, v. 69, p. 216-223.

Marsh, B.D., 1988, Crystal size distribution (CSD) in rocks and the kinetics and dynamics of crystallization: I. Theory: Contributions to Mineralogy and Petrology, v. 99, p. 277-291.

Marsh, B.D., 1998, On the interpretation of crystal size distributions in magmatic systems: Journal of Petrology, v. 39, p. 553-599.

Marshall, D., Anglin, C.D., 2004, $CO_2$-clathrate destabilization: a new model of formation for Molar-Tooth structures: Precambrian Research.

O'Connor, M.P., 1972, Classification and environmental interpretation of the cryptalgal organosedimentary "molar-tooth" structure from the Late Precambrian Belt-Purcell Supergroup: Journal of Geology, v. 80, p. 592-610.

Pollock, M.D., Kah, L.C., Bartley, J.K., 2006, Morphology of molar-tooth structures in Precambrian carbonates; influence of substrate rheology and implications for genesis: Journal of Sedimentary Research, *in pres.*

Pope, M.C., Bartley, J.K., Knoll, A.H., Petrov, P.Y., 2003, Molar-tooth structures in calcareous nodules, Early Neoproterozoic Burovaya Formation, Turukhansk Region, Siberia: Sedimentary Geology, v. 158, p. 592-610.

Pratt, B.R., 1998, Molar-tooth structure in Proterozoic carbonate rocks: origin from synsedimentary earthquakes, and implications for the nature and evolution of basins and marine sediment: Geological Society of Americas Bulletin, v. 110, p. 1028-1045.

Pratt, B.R., 2001, Oceanography, bathymetry and syndepositional tectonics of a Precambrian intracratonic basin: integrating sediments, storms, earthquakes, and tsunamis in the Belt Supergroup (Helena Formation, ca. 1.45 Ga), western North America: Sedimentary Geology, v. 141-142, p. 371-394.

Sawada, K., Takeshi, O., Toshio, S., 1990, The distribution coefficients of Mg ion between $CaCO_3$ polymorphs and solution and the effects on the formation and transformation of $CaCO_3$ in water: Journal of Crystal Growth, v. 106, p. 393-399.

Shields, Graham A., 2002, Molar-tooth microspar: a chemical explanation for its disappearance ~ 750 Ma: Terra Nova, v. 14, p. 108-113.

Smith, G.A., 1968, The origin and deformation of some "molar-tooth" structures in the Precambrian Belt-Purcell Supergroup: Journal of Geology, v. 76, p. 426-443.

Urmos, J., Shamra, S.K., Mackenzie, F.T., 1991, Characterization of some biogenic carbonates with Raman spectroscopy: American Mineralogist, v. 76, p. 641-646.

Young, G.M., Long, D.G.F., 1977, Carbonate sedimentation in a late Precambrian shelf sea, Victoria Island, Canadian Arctic Archipelago: Journal of Sedimentary Petrology, v. 47, p. 943-955.

## VITA

John Curtis Crawford was born in Knoxville, Tennessee on June 4, 1970. He was raised in Knoxville and graduated from Bearden High School in 1988. From there, he went to the University of Tennessee, Knoxville where he received a B.S. in Communications in 1996. After graduating, John accepted employment with Franklin's printing. In June 2000, he began pursuing a B.S. degree in geological sciences at the University of Tennessee, Knoxville. In 2003, John began pursuing a M.S. in geological sciences at the University of Tennessee. In 2005, John went down to Georgia, he was lookin' for a soul to steal. He was in a bind, and he was way behind, and he was willin' to make a deal…